

**ELECTRONIC, VIBRATIONAL AND
TRANSPORT PROPERTIES OF QUASI-ONE
DIMENSIONAL TRANSITION METAL
DICALCOGENIDE STRUCTURES**

**A Thesis Submitted to
the Graduate School of Engineering and Sciences of
İzmir Institute of Technology
in Partial Fulfillment of the Requirements for the Degree of**

MASTER OF SCIENCE

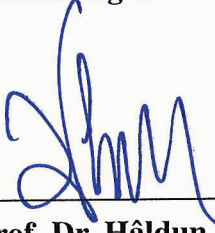
in Physics

**by
Elif ÜNSAL**

**December 2019
İZMİR**

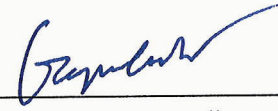
We approve the thesis of **Elif ÜNSAL**

Examining Committee Members:



Prof. Dr. Hâldun SEVİNÇLİ

Department of Materials Science and Engineering, İzmir Institute of Technology



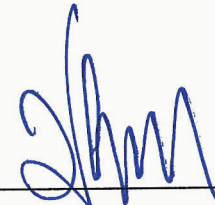
Assoc. Prof. Dr. Özgür ÇAKIR

Department of Physics, İzmir Institute of Technology



Assoc. Prof. Dr. Ümit AKINCI


Department of Physics, Dokuz Eylül University



Prof. Dr. Hâldun SEVİNÇLİ

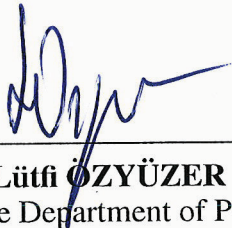
Supervisor, Department of Materials
Science and Engineering
İzmir Institute of Technology

17 December 2019



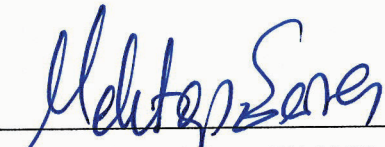
Prof. Dr. R. Tuğrul SENGER

Co-supervisor, Department of Physics
İzmir Institute of Technology



Prof. Dr. Lütfi ÖZYÜZER

Head of the Department of Physics
Physics



Prof. Dr. Mehtap EANES

Dean of the Graduate School of
Engineering and Sciences

ACKNOWLEDGMENTS

I appreciate Prof. Dr. R. Tuğrul Senger and Prof. Dr. Hâldun Sevinçli for their patience, valuable guidance and encouragement throughout my study.

I would like to thank the committee members of my thesis, Assoc. Prof. Dr. Özgür ÇAKIR and Assoc. Prof. Dr. Ümit AKINCI, for their participations and proofreading.

I am deeply grateful to my family, Hülya, Cengiz, Pankek and Fuzuli, for their endless support and love.

I am also deeply grateful to my better half, Merve Demir, for sparing her time whenever I need her. Her support, encouragement and ideas have been great contributors in my life.

I would like to express my gratitude to my dearest friends, Ahmet Azgın, Gökhan Öztarhan, and Gün Deniz Akkoç, for their patience, valuable discussions and the wonderful times we shared.

This work was supported by the Scientific and Technological Research Council of Turkey (TÜBİTAK), Grant No. 117F131 and Grant. No. 117F480.

ABSTRACT

ELECTRONIC, VIBRATIONAL AND TRANSPORT PROPERTIES OF QUASI-ONE DIMENSIONAL TRANSITION METAL DICHALCOGENIDE STRUCTURES

Thermoelectric materials have attracted great attention due to their ability to convert heat to electrical energy. As the application area of nanoscience expands, nanostructuring becomes a promising approach for enhancing thermoelectric properties. In this thesis, thermoelectric enhancement of the T-phase HfSe₂ structures is studied via nanostructuring. Density functional theory (DFT) based electronic and vibrational spectra of two-dimensional (2D) and quasi-one dimensional T-phase HfSe₂ structures are investigated and their ballistic thermoelectric transport properties are examined within the Landauer formalism. For the first time, it was reported that the nanoribbons of the T-phase HfSe₂ are dynamically stable and semiconducting materials. They have promising thermoelectric properties. We reported the enhancement of the p-type ZT parameter of T-phase HfSe₂ at both low and high temperatures. Moreover, the width dependency of the thermoelectric properties of the nanoribbons are studied.

ÖZET

KUASI BİR BOYUTLU GEÇİŞ METALİ YAPILARIN ELEKTRONİK, TİTREŞİMSSEL VE TAŞINIM ÖZELLİKLERİ

Termoelektrik malzemeler, ısı ve elektrik enerjisi arasında çevirim yapabildikleri için büyük ilgi çekmektedirler. Nanobilimdeki uygulama alanları genişledikçe, termoelektrik verimliliği artırmada, nanoyapılandırma umut vadeden bir yaklaşım olmuştur. Bu çalışmada, T-fazına sahip HfSe₂ yapısının termoelektrik verimliliğinin nanoyapılandırma ile artırılması çalışılmıştır. Yoğunluk fonksiyoneli (DFT) teorisi kullanılarak, iki boyutlu ve kuasi-bir boyutlu malzemelerin elektronik ve titreşimsel bant yapıları incelenmiş ve balistik termal taşınım özellikleri Landauer formalizmi kullanılarak elde edilmiştir. İlk defa bu çalışmada, T-fazı HfSe₂'nin kuasi-bir boyutlu nanoşeritleri incelenmiştir. Dinamik olarak kararlı bulunmuşlardır ve her bir malzeme yarı iletken karaktere sahiptir. Hem düşük, hem de yüksek sıcaklıklarda p-type ZT parametresinde artış hesaplanmıştır. Nanoşeritlerin kalınlıklarına bağlı termoelektrik özellikleri de incelenmiştir.

TABLE OF CONTENTS

LIST OF FIGURES	viii
LIST OF TABLES	x
LIST OF ABBREVIATIONS	xi
CHAPTER 1. INTRODUCTION	1
CHAPTER 2. DENSITY FUNCTIONAL THEORY	3
2.1. Thomas-Fermi-Dirac Model	3
2.2. Hohenberg-Kohn Theorems	4
2.3. Many-body Hamiltonian	4
2.4. Hartree-Fock Approximation	6
2.5. Kohn-Sham Equations	7
2.6. Exchange-Correlation Functionals	8
2.6.1. Local Density Approximation	9
2.6.2. Generalized Gradient Approximation	9
2.6.3. Heyd-Scuseria-Ernzerhof Hybrid Functional	10
2.7. Simulation Package Used	11
CHAPTER 3. QUANTUM TRANSPORT	13
3.1. Electronic Transport	13
3.1.1. Transport Regimes	13
3.1.2. Landauer Formalism and Total Current	14
3.2. Phononic Transport	19
3.3. Thermoelectric Properties	22
CHAPTER 4. STRUCTURAL, ELECTRONIC, VIBRATIONAL AND TRANSPORT PROPERTIES OF HfSe ₂ STRUCTURES	28
4.1. Structural Properties	28
4.2. Electronic Properties	29
4.3. Vibrational Properties	30

4.4. Thermoelectric Properties.....	31
CHAPTER 5. CONCLUSIONS	37
REFERENCES	38
APPENDIX A. NANORIBBON STRUCTURES OF T-HfSe ₂	44

LIST OF FIGURES

<u>Figure</u>	<u>Page</u>
Figure 2.1. Flow-chart of DFT-based self-consistent calculations are given.	12
Figure 3.1. A device in equilibrium with two reservoirs (R_L and R_L) is shown in the left panel. In equilibrium, R_L and R_R have same chemical potential μ . When a applied bias V_{bias} is applied the equilibrium is disturbed as shown in right panel and the chemical potentials of the reservoirs differ from each other.	15
Figure 3.2. A square potential barrier in one-dimensional (1D) system in equilibrium state is shown with red dashed line. When a bias voltage V_{bias} is applied, the potential of the right reservoir is changed and a voltage drop ΔV occurs (shown as black line). In Landauer formalism, the V_{bias} is assumed to be small which means ΔV is much smaller than the potential barrier. Thus the transmission function can be calculated for the square barrier in which transmission function has a constant value in the energy range where the transport takes place (Brocks, 2005; Datta, 2009).	15
Figure 3.3. The band structure of a semiconductor is shown on the left. Fermi level is set to zero. In the right panel, Lorenz number L at 300 K of a semiconductor is given as a function of chemical potential. Red dashed lines represent the degenerate (Sommerfeld) limit which has a value of $2.44 \times 10^{-8} W \Omega K^{-2}$ and green dashed line is the lower limit with a value of approximately $0.75 \times 10^{-8} W \Omega K^{-2}$	26
Figure 4.1. The geometries of the single layer (SL-HfSe ₂) and nanoribbons (NRs) are represented. (a) Blue and orange lines show the armchair and zigzag directions, respectively. (b) Atoms marked with red circles define the number of atoms in the width of NR, n . In (c) and (d), NRs with two different type of edges are illustrated.	29
Figure 4.2. Electronic band structures for (a) single layer (SL-HfSe ₂) and (b)-(e) nanoribbon (NR) structures with $n=6,7,12,13$ are presented. The Fermi level is set to zero. (f) NRs with even n have glide reflection symmetry, while NRs with odd n have mirror image symmetry. (g) As the width of the NR is getting wider, the energy band gap value converges to the band gap value of SL-HfSe ₂	30

<u>Figure</u>	<u>Page</u>
Figure 4.3. Phonon band spectra of the single layer (SL-HfSe ₂) and nanoribbon (NRs) structures are presented.	31
Figure 4.4. From left to right, thermoelectric figure of merit (ZT) as a function of temperature, the phonon thermal conductance (κ_p) and ZT as a function of chemical potential (μ) are given for nanoribbon (NR) with $n=12$	32
Figure 4.5. In the top panel, variation of n-type thermoelectric figure of merit (ZT) with the width of the nanoribbon (NR) and ZT as function of temperature for NRs with even and odd n are given. p-type ZT values are given in the bottom panel.	33
Figure 4.6. For the nanoribbons (NRs) with $n=9$, $n=11$ and $n=13$, the electronic band and their transmission spectra are given in the first row. Power factor and thermoelectric figure of merit (ZT) are shown in the second and third rows, respectively.	34
Figure 4.7. In the left panel, the phonon thermal conductance (κ_p) of the single layer T-HfSe ₂ (SL-HfSe ₂) and nanoribbon (NR) structures are given at 300 and 800K. In the right panel, κ_p of NR structures are given as a function of temperature. κ_p values are the scaled values with respect to the width of the NRs. κ_p values of SL-HfSe ₂ are from the study of Özbal et al. (2019).	35
Figure 4.8. Lorenz number L of the nanoribbons (NRs) is given as a function of chemical potential μ at 300 K. Red dashed lines represent the degenerate (Sommerfeld) limit which has a value of $2.44 \times 10^{-8} W \Omega K^{-2}$. V_{max} and C_{min} are the valence band maximum and conduction band minimum values, respectively.	36

LIST OF TABLES

<u>Table</u>		<u>Page</u>
Table 4.1.	Calculated parameters of the single layer (SL-HfSe ₂) and nanoribbon (NR) structures are; the lattice constant b ; the thickness of the structures, t ; the width of the structures; w , the energy band gaps calculated with PBE and PBE+HSE06 functionals, E_g^{PBE} and $E_g^{PBE+HSE06}$, respectively.	28
Table 4.2.	The calculated parameters of the single layer (SL-HfSe ₂) (Özbal et al., 2019) and nanoribbon structures are; p- and n-type Seebeck coefficient, S ; power factor, P , thermoelectric figure of merit, ZT , and phonon thermal conductance per nm, κ_p	32

LIST OF ABBREVIATIONS

2D	Two-dimensional
1D	One-dimensional
TMD	Transition Metal Dichalcogenide
DFT	Density Functional Theory
LDA	Local Density Approximation
GGA	Generalized Gradient Approximation
MGGA	Meta-generalized Gradient Approximation
HSE06	Heyd-Scuseria-Ernzerhof (2006)
SR	Short Range
LR	Long Range
VASP	Vienna ab initio Simulation Package
NR	Nanoribbon
SL-HfSe ₂	Generalized Gradient Approximation

CHAPTER 1

INTRODUCTION

Following the the synthesis of graphene (Novoselov, 2004), the family of two-dimensional (2D) materials have expanded and they have been the focus of the interest. In this study, we focused on the transition metal dichalcogenides (TMDs) (Mak, 2010; Kong, 2013; Huang, 2014) due to their unique physical properties and potential in nano-electronics, nano-optics and energy conversion applications. The bulk forms of TMDs are composed of atomically thin sub-layers bonding via weak van der Waals forces while in-plane bonding of the sub-layers are strong which makes them highly stable materials and they exhibit mechanical flexibility (Castellanos-Gomez A, 2012; Velusamy DB, 2015). Having a high chemical stability and controllable synthesis are important for the device applications and 2D TMDs meet these requirements (Zhang and He, 2019; Yu and Chang, 2015). The electronic characteristics of TMDs varies ranging from insulating, semiconducting, half- and semi- metallic to superconducting. Having a wide range of band gaps enables these materials to be used in electronic and optic device applications and it is known that their band gaps are layer-dependent tunable (Wang, 2012). Moreover, TMDs have lower lattice thermal conductivity which make them practical for the applications, such as thermoelectric cooling devices (Zhang, 2015; Sahoo et al., 2013).

Thermoelectric materials have an ability of a conversion between heat and electrical energy via thermoelectric effect. Thermoelectric effect determines the relation between the temperature and the voltage differences that occur between the two edges of a material. Seebeck and Peltier are examples of the thermoelectric effects and they have been known and studied for a long time. In Seebeck effect, a temperature gradient of a metal or a semiconducting material causes a potential difference between the two ends of the material. On the contrary, in Peltier effect, the electrical energy is used to drive heat by applying bias which results in a temperature difference between the two ends of the device. This is used for the cooling. For instance, the working principle of a thermocouple is based on Seebeck effect and it can be used for converting the heat loss to electrical energy also known as the power generation.

Increasing the efficiency of the thermoelectric materials are important in device technologies. The efficiency to energy conversion of a thermoelectric material is measured with a dimensionless figure of merit, $ZT = \sigma S^2 T / \kappa$, where σ , S and κ are elec-

trical conductivity, Seebeck coefficient and total thermal conductivity, respectively and T is temperature. The total conductivity is defined as $\kappa = \kappa_{el} + \kappa_p$ where κ_{el} and κ are the thermal conductivities of electrons and phonons, respectively. An efficient thermoelectric material has a high Seebeck coefficient and electrical conductivity, and a low thermal conductivity. Typical ZT values are about 1 for commercial and reaches 3 or higher in laboratory conditions (Poudel and Ren, 2008; Mao and Ren, 2019; Xiao and Zhao, 2018). Therefore, in order to enhance the thermoelectric efficiency, the Seebeck coefficient and the electrical conductivity of the material can be increased or the total thermal conductivity can be reduced. However, according to Wiedemann-Franz law (Franz, 1853), the electrical thermal conductivity of electrons is linearly dependent to the electrical conductivity. Reducing the thermal conductivity of electrons leads to a decrease in the electrical conductivity. Thus, improving the Seebeck coefficient and reducing the phonon thermal conductance are mostly preferred for the enhancement of thermoelectric efficiency (G. J. Snyder, 2008).

Decreasing the phonon thermal conductance can be achieved via reducing the dimensions of the structure. As the dimension of a material is reduced, the surface scatterings occur more frequently which results in a decrease in the lattice thermal conductivity (Hicks and Dresselhaus, 1993a,b). Thus, enhancement in the material efficiencies can be achieved via nanostructuring (Balandin, 2011; H. Alam, 2013), such as generating heterostructures or reducing their dimensions via forming their nanoribbons, quantum dots etc.

In this study, we focused on the single layer T-phase HfSe_2 since it is recently reported that its 2D structure is air-stable and fabricated down to three-layer thickness (Mleczko and Pop, 2017). Moreover, among TMDs, Hf based structures have relatively higher ZT values and the calculated values at low (high) temperatures are close to one (two) (Özbal et al., 2019). Herein, we aimed to enhance the thermoelectric properties of the T-phase HfSe_2 structures via nanostructuring. By performing density functional theory-based ab initio calculations, first, we investigated the electronic and vibrational spectra of two-dimensional (2D) and quasi-one dimensional T-phase HfSe_2 structures. For the nanoribbon structures, ballistic transport properties are analyzed within the Landauer formalism. We reported that the enhancement of the p-type ZT parameter of T-phase HfSe_2 at both low and high temperatures. Moreover, the width dependence of the thermoelectric properties of the nanoribbons are studied. With their enhanced thermoelectric properties, quasi-one dimensional HfSe_2 structures are promising candidates for the thermoelectric device applications.

CHAPTER 2

DENSITY FUNCTIONAL THEORY

Density Functional Theory (DFT) is a computational method which is beneficial for investigating properties of many-body systems. In reality, the electrons are dependent with each other and nuclei, thus the wave function of N-electron system is not separable and the degrees of freedom of the system is $3N$. Solving the Schrödinger equation for the wave function of such a system is impossible even for its ground state. Instead of the many-body wave function, in principle, density functional theory is based on a position-dependent ground state electron density:

$$n(\vec{r}) = N \int |\psi(\vec{r}, \vec{r}_2, \dots, \vec{r}_N)|^2 d\vec{r}_2 d\vec{r}_3 \dots d\vec{r}_N \quad (2.1)$$

where $\psi(\vec{r}, \vec{r}_2, \dots, \vec{r}_N)$ is the many-body wave function and \vec{r}_i 's are the positions of the electrons. The ground state energy of the system is a functional of the density written in terms of the wave function. The advantageous part of DFT is that the method gives accurate solutions for large and complex systems and it also lowers the computational cost for such systems by reducing the degrees of freedom by defining the density.

To understand the logic of DFT, it is beneficial to start from the Thomas-Fermi-Dirac model which is known as the root of DFT. Then we will continue with Hohenberg-Kohn theorems which make DFT possible and Kohn-Sham ansatz that provides a way to construct approximate functionals for many-electron systems.

2.1. Thomas-Fermi-Dirac Model

Llewellyn Thomas and Enrico Fermi have developed a theory for the electronic structure of systems which include many particles (Fermi, 1927) for the first time. They realized that the ground state energy of the free Fermi gas, can be written in terms of a function of electron density. Functional offered by Thomas and Fermi neglect the correlated motion of the electrons in a quantum mechanical system. The electrons influence

the movements of each other and the measure this influence on electrons leads to correlation energy which has a form of Coulombic potential. Thomas and Fermi also ignored the exchange interaction of electrons. Considering the Pauli exclusion principle, the electrons those have same spin are affected from each other repulsively when they are close to each other. After Thomas and Fermi offered their functional, Dirac (Dirac, 1930) improved this functional with adding the exchange-correlation terms.

2.2. Hohenberg-Kohn Theorems

Hohenberg and Kohn proved that the ground state energy is a unique functional of density which makes DFT possible (Hohenberg and Kohn, 1964). The many-electron wave function contains all physical information of the system, thus the density functional contains that information. The two different many-electron systems only differ in the external potential. Therefore, two different potential cannot give the same density. If the ground state density of a many-electron system is known, one can calculate the external potential of the system.

Hohenberg and Kohn also stated that the energy functional can be defined in terms of ground-state density which minimizes the functional to its global minimum and the energy of the system varies with the density.

2.3. Many-body Hamiltonian

Considering the construction of the many-body Hamiltonian, there are three kinds of interaction between the particles of interest.

- 1) **Nucleus-nucleus interaction:** According to Born-Oppenheimer (Born and Oppenheimer, 1927), nuclei can be treated as classical particles. Thus, they are assumed to be static. Even with this simplification, calculating the potential energy caused by the interactions of nuclei is challenging. In order to handle the calculation of long-range Coulombic interaction in the periodic systems, one can utilize Ewald summation (Ewald, 1921). As a result of this interaction, the obtained term for N_n number of nuclei is:

$$\hat{V}_{nn} = + \frac{e^2}{4\pi\epsilon_0} \frac{1}{2} \sum_I^{N_n} \sum_{J \neq I}^{N_n} \frac{Z_I Z_J}{|\vec{R}_I - \vec{R}_J|} \quad (2.2)$$

where e and ϵ_0 are the charge of the electron and the vacuum permittivity, respectively. Z_I and Z_J are the atomic numbers of the I^{th} and J^{th} nuclei. \vec{R}_I and \vec{R}_J represents the positions of nuclei.

- 2) **Nucleus-electron interaction:** Since the nuclei are taken as static particles, potential of nucleus is like a single-body external potential acting on an electron.

$$\hat{V}_{ne} = -\frac{e^2}{4\pi\epsilon_0} \sum_i^{N_e} \sum_I^{N_n} \frac{Z_I}{|\vec{r}_i - \vec{R}_I|} \quad (2.3)$$

where N_e is the number of electrons in the system and \vec{r}_i denotes the position of i^{th} electron. Minus sign is a result of the attractive interaction between nucleus and electron. In order to calculate the potential of the nuclei, for practicality, pseudopotentials are used which will be mentioned later.

- 3) **Electron-electron interaction:** The complexity of the many-electron system arises mostly due to this term because all electrons are affected from each other.

$$\hat{V}_{ee} = +\frac{e^2}{4\pi\epsilon_0} \frac{1}{2} \sum_i^{N_e} \sum_{j \neq i}^{N_e} \frac{1}{|\vec{r}_i - \vec{r}_j|} \quad (2.4)$$

This term has a positive sign since the interaction is repulsive. Coefficient of $1/2$ is important for avoiding the double-counting, and in order to prevent the self-interaction of particles, $J \neq I$ and $j \neq i$ terms are considered for \hat{V}_{nn} and \hat{V}_{ee} .

In Hamiltonian, the kinetic energy term is assumed to only come from the motion of the electrons.

$$\hat{T}_e = \frac{\hbar^2}{2m_e} \sum_i^{N_e} \nabla_i^2 \quad (2.5)$$

where \hbar and m_e denotes the Planck's constant divided by 2π and the electron mass, respectively.

In this work, the materials of interest are non-magnetic. Therefore, the spin part will not be included since the solutions remains almost unchanged. Taking into account all above, the Hamiltonian of a system, which has N_e number of electrons and N_n number of nuclei, is constructed as :

$$\hat{H} = -\frac{\hbar^2}{2m_e} \sum_i^{N_e} \nabla_i^2 + \frac{e^2}{4\pi\epsilon_0} \left[-\sum_i^{N_e} \sum_I^{N_n} \frac{Z_I}{|\vec{r}_i - \vec{R}_I|} + \frac{1}{2} \sum_i^{N_e} \sum_{j \neq i}^{N_e} \frac{1}{|\vec{r}_i - \vec{r}_j|} + \frac{1}{2} \sum_i^{N_n} \sum_{J \neq I}^{N_n} \frac{Z_I Z_J}{|\vec{R}_I - \vec{R}_J|} \right] \quad (2.6)$$

2.4. Hartree-Fock Approximation

Hartree-Fock method is developed for fulfilling the anti-symmetry requirement for the many-body fermion wave-function (Fock, 1930). General form of the wave function of many-body system is defined as the product of occupied orbitals which is also known as the Hartree product (Hartree, 1928). However, Hartree product fails when a system of many electrons (fermions) is considered. A fermionic system obeys the Pauli exclusion principle in which a wave function describing fermions are anti-symmetric with respect to the interchange of their spins. The Pauli exclusion principle is satisfied by defining the wave function of system of N electrons with the Slater determinant.

$$\Phi(\vec{x}_1 \dots \vec{x}_N) = \frac{1}{\sqrt{N!}} \begin{vmatrix} \phi_1(\vec{x}_1) & \dots & \phi_N(\vec{x}_1) \\ \vdots & \ddots & \vdots \\ \phi_1(\vec{x}_N) & \dots & \phi_N(\vec{x}_N) \end{vmatrix} \quad (2.7)$$

Form of the orbitals can be calculated as a result of the energy minimization procedure by utilizing the variational method. This method allows to calculate the ground state energy approximately. In this method, a trial wave function which depends on some variational parameters is assigned for the related system. Then these parameters are adjusted until the energy of the wave function is minimized. An exact solution of wave function can be obtained by calculating the expectation value of the Hamiltonian for this variational wave function.

$$E[\textit{variational parameter}] = \frac{\langle \Phi | \hat{H} | \Phi \rangle}{\langle \Phi | \Phi \rangle}, \quad (2.8)$$

with a constraint of $\langle \Phi | \Phi \rangle = 1$.

2.5. Kohn-Sham Equations

The total energy is minimized with respect to the density, through the Hohenberg-Kohn theorems which show that the minimum energy is the ground state energy. While minimizing the energy dealing with the kinetic energy of interacting many-electron system is challenging. In this case, fictitious and distinguishable Kohn-Sham orbitals $\phi_i(\vec{r})$ are defined (W. Kohn, 1965).

$$n(\vec{r}) = \sum_{i=1}^{N_e} |\phi_i(\vec{r})|^2 \quad (2.9)$$

The total energy can be minimized with respect to these orbitals instead of the density (Martin, 2004). Differentiation can be done by using the chain rule for functional derivative except for the kinetic energy term. Since the kinetic energy of the system is divided into two parts which are kinetic energy of the orbitals and the correction term, the terms of orbitals can be differentiated directly in terms of the orbitals. Moreover, $\phi_i^*(\vec{r})$ will be used instead of $\phi_i(\vec{r})$ since $\phi_i(\vec{r})$ is defined as real function. Therefore, the choice of conjugate does not alter the solution which is formed as seen below.

$$\frac{\delta E_e}{\delta \phi_i^*(\vec{r})} = \frac{\delta T_s}{\delta \phi_i^*(\vec{r})} + \left[\frac{\delta E_{ext}}{\delta n(\vec{r})} + \frac{\delta E_{Hartree}}{\delta n(\vec{r})} + \frac{\delta E_{xc}}{\delta n(\vec{r})} \right] \frac{\delta n(\vec{r})}{\delta \phi_i^*(\vec{r})} = 0 \quad (2.10)$$

E_e is the energy of the electronic system, which indicates that the energy obtained from the nucleus-nucleus interaction is omitted and this term is taken to be constant. E_{ext} and E_{xc} are the external and the exchange-correlation energies, respectively. $E_{Hartree}$ represents the Coulombic potential due to the electron-electron interaction. The Eq. 2.10 is same as the derivation of the Schrödinger equation.

$$-\frac{1}{2}\nabla^2\phi_i(\vec{r}) + \left[V_{ext} + \int \frac{n(\vec{r}')}{|\vec{r}-\vec{r}'|} d\vec{r}' + \epsilon_{xc}[n] + n(\vec{r})\frac{\delta\epsilon_{xc}[n]}{\delta n(\vec{r})} \right] \phi_i(\vec{r}) = \varepsilon_i\phi_i(\vec{r}) \quad (2.11)$$

where,

$$\int \frac{n(\vec{r}')}{|\vec{r}-\vec{r}'|} d\vec{r}' = V_{Hartree} \quad \text{and} \quad \epsilon_{xc}[n] + n(\vec{r})\frac{\delta\epsilon_{xc}[n]}{\delta n(\vec{r})}\phi_i(\vec{r}) = V_{xc} \quad (2.12)$$

Eq. 2.11 is known as the Schrödinger-like Kohn-Sham equations written in Hartree units in which m_e , e , \hbar , and $1/(4\pi\epsilon_0)$ are taken as equal to one. The interaction between the nuclei and electrons are replaced by pseudopotential included in V_{ext} term. For a known exact exchange-correction energy, Kohn-Sham equations can be solved numerically and this leads to the exact ground state density of the electronic system. Solving the Eq. 2.11 simultaneously gives the solutions of the many-body system in term of the single-body system. The summation of all potential terms ($V_{ext} + V_{Hartree} + V_{xc}$) in Eq. 2.11 are called effective potential (also known as the Kohn-Sham potential). Taking the derivative of the potential with respect to the orbitals leads to the solution of orbitals. This problem can be handled by self-consistent solutions of the Kohn-Sham equations (Toffoli, 2012).

2.6. Exchange-Correlation Functionals

Potential energy term of electron-electron interaction, V_{ee} is written in terms of two-particle density which gives the probability of both electron at \vec{r} and electron at \vec{r}' . However, this probability cannot be solved easily. Therefore, these terms can be constructed with two different densities and also with an extra term which comes from the correction.

$$V_{ee} = \frac{1}{2} \int \int d\vec{r} d\vec{r}' \frac{n(\vec{r})n(\vec{r}')}{|\vec{r}-\vec{r}'|} + \Delta V_{ee} \quad (2.13)$$

When the density is defined in terms of the Kohn-Sham orbitals, kinetic energy term has the form as follows.

$$T_{KS} = -\frac{1}{2} \sum_i^{N_e} \int \phi_i^*(\vec{r}) \nabla^2 \phi_i(\vec{r}) d\vec{r} \quad (2.14)$$

Calculating the kinetic energy of these orbital is still not the solution, because it belongs to the fictitious system. The essential kinetic energy of the system is formed as seen below.

$$T_{ee} = -\frac{1}{2} \sum_i^{N_e} \int \psi^*(\vec{r}_1, \dots, \vec{r}_N) \nabla^2 \psi(\vec{r}_1, \dots, \vec{r}_N) d\vec{r}_1 \dots d\vec{r}_N \quad (2.15)$$

$$= -\frac{1}{2} \sum_i^{N_e} \int \phi_i^*(\vec{r}) \nabla^2 \phi_i(\vec{r}) d\vec{r} + \Delta T_{ee} \quad (2.16)$$

The ΔV_{ee} term in Eq. 2.13 and the ΔT_{ee} in Eq. 2.16 comes from the exchange-correlation of the electrons and they can be written as seen below.

$$E_{xc} = \Delta V_{ee} + \Delta T_{ee} = \int n(\vec{r}) \epsilon_{xc}(n) d\vec{r} \quad (2.17)$$

2.6.1. Local Density Approximation

As mentioned in previously, Dirac introduced a exchange functional for the uniform electron gas. The exchange energy is defined as the Coulomb interaction energy between the electron and its exchange hole. Exchange part of $\epsilon_{xc}^{hom}(n(\vec{r}))$ is an exact result of Hartree-Fock and the correlation part is calculated from Quantum Monte Carlo data. Within this approximation, exchange-correlation functional of a system depends only on the local density at a given point.

$$E_{xc}^{LDA} = \int d\vec{r} n(\vec{r}) \epsilon_{xc}^{hom}(n(\vec{r})), \quad (2.18)$$

where $n(\vec{r})$ is the homogeneous electron gas at the density and $\epsilon_{xc}^{hom}(n(\vec{r}))$ is its exchange correlation energy density.

2.6.2. Generalized Gradient Approximation

In local density approximation (LDA) system is assumed to be homogeneous; however, in reality, density of the system varies slowly over space due to the screening of the nuclei. In order to take this into account, a function f is defined in terms of density and also its gradient and the exchange-correlation functional is defined by this function.

$$E_{xc}^{GGA} = \int d\vec{r} f(n(\vec{r}), \nabla n(\vec{r})), \quad (2.19)$$

When the second-order derivatives of the density are included in the function f , one obtains the meta-generalized gradient approximation (MGGA).

2.6.3. Heyd-Scuseria-Ernzerhof Hybrid Functional

Hybrid functional is a sort of approximation to exchange-correlation energy functional which is a combination of certain amount of exact exchange from Hartree-Fock theory and local or semi-local density functional.

The exact Hartree-Fock exchange calculation causes computational cost particularly for the metallic systems due to the divergence of the derivative of the orbital energies with respect to k (N. W. Ashcroft, 1975a). The divergence originates from the Fourier transform of the Coulomb potential ($4\pi/k^2$). If the screened potential is shorter than a range of $1/r$ Coulomb potential, the divergence is suppressed. In order to eliminate the divergence, Heyd *et al.* proposed a hybrid functional based on a screened Coulomb potential only for the exchange interaction in which the long-range part of the exact exchange is screened (J. Heyd, 2003). Later, Krukau *et al.* enhanced this hybrid functional known as HSE06. In HSE functional, the Coulomb potential is separated into two parts, short-range (SR) and long-range (LR):

$$\frac{1}{r} = \frac{1 - \text{erf}(\omega r)}{r} + \frac{\text{erf}(\omega r)}{r}, \quad (2.20)$$

where first and second part are SR and LR parts, respectively and erf is error function. ω is the screening parameter that defines the separation range. The hybrid exchange functional is:

$$E_{XC}^{HSE} = \frac{1}{4}E_X^{HF,SR}(\omega) + \frac{3}{4}E_X^{PBE,SR}(\omega) + E_X^{PBE,LR}(\omega) + E_C^{PBE}, \quad (2.21)$$

where $E_X^{HF,SR}(\omega)$ is the exact exchange for short-range, $E_X^{PBE,SR}(\omega)$ and $E_X^{PBE,LR}(\omega)$ are the PBE exchange functional for short-range and long-range, respectively. E_C^{PBE} is the PBE correlation energy.

2.7. Simulation Package Used

In this work, first-principle calculations based on DFT were performed as implemented in the Vienna ab initio Simulation Package (VASP) (Kresse and Hafner, 1993; Kresse and Furthmüller, 1996)

In the beginning, it is assigned an initial guess for the electron density required for effective potential calculation, the diagonalization of the Kohn-Sham equations, and the subsequent values of density, so the total energy. If the convergence criterion cannot be reached, the numerical procedure is relaunched with the last $n(r)$ as the initial guess. Otherwise, the output quantities are computed. A flow chart of the iteration scheme is given in Fig. 2.1.

In this study, we used pseudopotential approximation supplied with VASP; therefore, a brief information about pseudopotential approximation will be beneficial. Pseudopotentials are generated to replace the deep Coulombic interaction near the nuclei to avoid the technical difficulties which it poses. In creating a pseudopotential, one assumes that the core electrons of the atoms are included in the nucleus and their effects are replaced with an effective potential. Especially for large atoms with many electrons, this approximation shortens the calculations even if the calculations are computational. Procedure of generating the pseudopotentials begins with using the Kohn-Sham approach. By using Kohn-Sham orbitals, a distinction between the valence and core electronic states are made. The effects of the core states are switched by a new potential which is derived in for an isolated atomic configuration. While the real atomic states oscillate rapidly around the core states, this new potential provides to make valence states smoother due to screening of the ionic potential by the core electrons (Toffoli, 2012).

Herein, the Perdew-Burke-Ernzerhof (PBE) form of generalized gradient approximation (GGA) was adopted (Perdew et al., 1996) in order to describe the exchange-

correlation energy, and HSE06 (A. V. Krukau, 2006) hybrid functional was used for the band gap estimation.

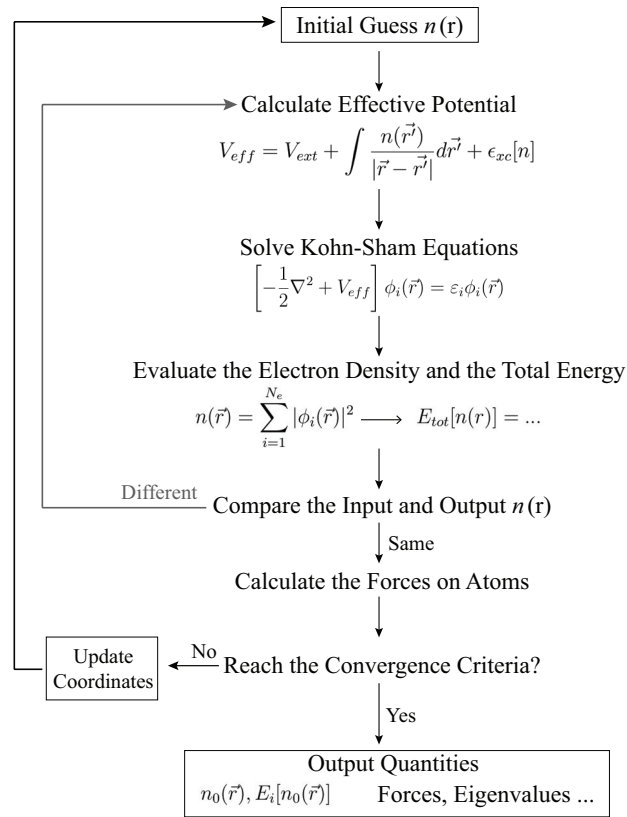


Figure 2.1. Flow-chart of DFT-based self-consistent calculations are given.

CHAPTER 3

QUANTUM TRANSPORT

Quantum transport deals with the conduction of the electrons in mesoscopic scale, an intermediate scale in which the materials with nano-scaled dimensions and of materials measuring micrometers.

In this chapter, a detailed information about formalism that we used for the calculation of electronic and phononic transport will be given. Herein, we used Landauer formalism for the electronic transport, and a heuristic Landauer-type heat current formula is utilised for the phononic transport.

3.1. Electronic Transport

Within electronic transport problem, there are several methods depending on the length scales. In this thesis, we investigated the quasi-one dimensional materials participated in ballistic regime. Therefore, a brief information about the length scales will be given, and then the ballistic transport of electrons and phonons will be explained in detail.

3.1.1. Transport Regimes

Comparison between the size of the structure and the average distance between scattering events (or mean free path of the carrier) is a key for the determination of the electronic transport regime (L. E. F. F. Torres, 2014). In ballistic regime, both width and length of the structure are smaller than the mean free path of the carrier. In this case, elastic scatterings from the boundaries of the structure identify the transport properties. Therefore, the structure geometry take an important role in the such kind of transport.

In diffusive regime, mean free path of the carrier is much smaller than the size of the sample; therefore, the carrier dwells in the sample and goes through many collisions. In this case, the scattering from impurities is influential for the determination of transport properties.

There is also another regime, Anderson localization regime, in which again the

length of the structure is larger than the mean free path of the carrier. In this case, electrons are localized due to the potential of impurities which causes an exponential relation between the resistance and the length of the structure ($R \propto e^{-L/L_0}$) (L. E. F. F. Torres, 2014). In this work, transport properties of quasi-one dimensional structures are investigated. Since their sizes are much smaller than the mean free path, the ballistic transport regime is considered.

3.1.2. Landauer Formalism and Total Current

Landauer (Landauer, 1957, 1970; Y. Imry, 1999) suggested that the electrical current can be considered as a result of charge carrier injection and the transmission probability of the carriers from drain to source. Landauer's suggestion is for the current through a conductor in two-lead systems. Later Büttiker (Büttiker, 1986) generalized his theory for multi-lead systems.

Let us start with the modeling of the two-lead system and the current flow in Landauer formalism (Datta, 2009, 2004; D. K. Ferry, 2009). Suppose a device is connected to two reservoirs which have chemical potentials (μ_L and μ_R) as represented in left panel of Fig. 3.1. Assume that the reservoirs (source and drain) are in the equilibrium state with the device channels (or available energy states). For the generation of the electric current through the channels of the device, there should be a difference between the chemical potentials of the reservoirs. If a small bias voltage ΔV is applied, the chemical potential of the drain decreases while the chemical potential of the source increases. The chemical potentials of source and drain are separated by $q\Delta V$ which is shown in right panel of Fig. 3.1. Each reservoir tends to be in the equilibrium with the device. While the source is ejecting electrons, the drain keeps collecting electrons back. Therefore, both of the reservoirs cannot reach the equilibrium with the device and the device is forced to be in a non-equilibrium state balancing between source and drain.

When the small bias is applied, the equilibrium between the device and the reservoirs is disrupted and the Fermi distributions of the source and drain differ from each other and the applied bias can be written as follows.

$$\Delta V = \frac{\mu_L - \mu_R}{q}, \quad (3.1)$$

where q is the charge of the carrier. The applied bias is assumed to be small which

means that $(\mu_L - \mu_R)$ is assumed to be much smaller than $k_B T$. Transmission function represents the average transition probability of an electron going from one reservoir to another. Within this assumption, transmission function of the charge carriers $\tau(E)$ has a constant value in the energy range where the transport takes place and it can be approximately calculated at an energy equal to the Fermi energy E_F . This is known as the linear response regime.

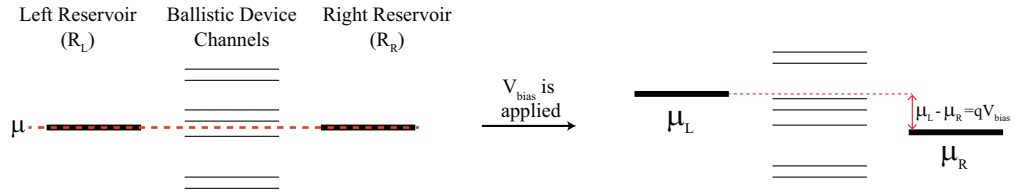


Figure 3.1. A device in equilibrium with two reservoirs (R_L and R_L) is shown in the left panel. In equilibrium, R_L and R_R have same chemical potential μ . When a applied bias V_{bias} is applied the equilibrium is disturbed as shown in right panel and the chemical potentials of the reservoirs differ from each other.

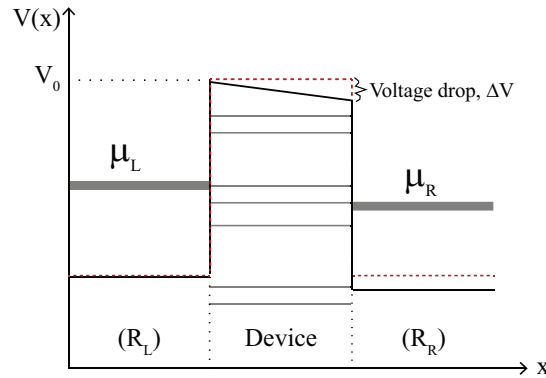


Figure 3.2. A square potential barrier in one-dimensional (1D) system in equilibrium state is shown with red dashed line. When a bias voltage V_{bias} is applied, the potential of the right reservoir is changed and a voltage drop ΔV occurs (shown as black line). In Landauer formalism, the V_{bias} is assumed to be small which means ΔV is much smaller than the potential barrier. Thus the transmission function can be calculated for the square barrier in which transmission function has a constant value in the energy range where the transport takes place (Brocks, 2005; Datta, 2009).

Transmission coefficient represents the average transition probability of an elec-

tron going from one reservoir to another. In linear response regime expression for current can be written as:

$$I = qnv\tau(E) = -env\tau(E) \quad (3.2)$$

where n and v are the density (concentration) and the velocity of charge carrier, respectively. n and v are defined as follows.

$$n = \int D(E)f(E)dE \quad (3.3)$$

$$v = \frac{1}{\hbar} \frac{\partial E}{\partial k} \quad (3.4)$$

where $D(E)$ is density between \vec{k} and $\vec{k} + d\vec{k}$ (or density per unit energy) and $f(E)$ is the the Fermi distribution function.

Since Landauer's formalism is obtained for one-dimensional system, let us start with the definition of density of wire-like one-dimensional ideal electron gas sample with a length of L . By definition, density of states is $d(N_{1D}/L)/dE$ where N_{1D} is the number of available electronic states:

$$N_{1D} = 2 \times \frac{2k_f}{\frac{2\pi}{L}} = \frac{2L}{\pi} \left(\frac{2mE}{\hbar^2} \right)^{1/2} \quad (3.5)$$

where the factor 2 is for the electron spin. $2k_f$ and $(2\pi)/L$ are the length of the Brillouin Zone and one electronic state, respectively. m and \hbar are the effective mass of the electrons and the Planck's constant (h) divided by 2π , respectively. N_{1D} is written in terms of the energy by using the parabolic relation between k and E . Then $D(E)$ in 1D can be written as follows.

$$D(E) = \frac{1}{\pi} \left(\frac{2m}{\hbar^2} \right)^{1/2} E^{-1/2} \quad (3.6)$$

Then the electron concentration of the conduction band is defined as:

$$\begin{aligned}
n &= \int_{\mu}^{\infty} D(E) f(E) dE \\
&= \int_{\mu}^{\infty} \left(\frac{(E - \mu)^{-1/2} (2m)^{1/2}}{\hbar\pi} \right) f(E - \mu) dE
\end{aligned} \tag{3.7}$$

By using the defined expressions of n and v in Eq. 3.2 the electrical current injected from left to right can be written as:

$$\begin{aligned}
I &= \left(-e \int_0^{\infty} D_L(E) f_L(E) v_L \tau(E) dE \right) + \left(e \int_0^{\infty} D_R(E) f_R(E) v_R \tau(E) dE \right) \\
&= \left(-e \int_0^{\infty} \left(\frac{(E - \mu_L)^{-1/2} (2m)^{1/2}}{\hbar\pi} \right) f_L(E) v_L \tau(E) dE \right) \\
&\quad + \left(e \int_0^{\infty} \left(\frac{(E - \mu_R)^{-1/2} (2m)^{1/2}}{\hbar\pi} \right) f_R(E) v_R \tau(E) dE \right)
\end{aligned} \tag{3.8}$$

in which the velocity is rewritten by using the parabolic relation between k and E $v_{L,R} = \sqrt{2(E - \mu_{L,R})/m}$. $f_L(E)$ and $f_R(E)$ are the Fermi distributions of the left and right reservoirs, respectively:

$$f_L(E) = \frac{1}{1 + e^{\frac{(E - \mu_L)}{k_B T}}} = f_0(E - \mu_L) \tag{3.9}$$

$$f_R(E) = \frac{1}{1 + e^{\frac{(E - \mu_R)}{k_B T}}} = f_0(E - \mu_R) \tag{3.10}$$

where k_B and T are the Boltzmann constant and temperature respectively. By using the expressions of n and v , the current equation can be modified as:

$$\begin{aligned}
I &= \frac{2e}{\hbar\pi} \left[- \int_0^{\infty} f_L(E) \tau(E) dE + \int_0^{\infty} f_R(E) \tau(E) dE \right] \\
&= \frac{e}{h} = \int_{-\infty}^{\infty} [f_L(E) - f_R(E)] \tau(E) dE
\end{aligned} \tag{3.11}$$

In general, the total current in Landauer formalism can be written as:

$$I = -\frac{2e}{h} \int_{-\infty}^{+\infty} d\varepsilon \tau(\varepsilon) [f_L(\varepsilon) - f_R(\varepsilon)], \quad (3.12)$$

As mentioned before, at the equilibrium state, both of the reservoirs have the same chemical potential and the current is zero. When there occurs small deviations from the equilibrium state, the current is proportional the applied bias. The applied bias is infinitesimal; thus, the distribution function, $f(\varepsilon)$, can be expanded around equilibrium values of the chemical potential and temperature by using the Taylor's series expansion.

$$f_i(\varepsilon) \cong f(\varepsilon) + \frac{\partial f(\mu)}{\partial \mu} (\mu - \mu_i) + \frac{\partial f(T)}{\partial T} (T - T_i), \quad (3.13)$$

where $i = L, R$. Let $(\varepsilon - \mu)/(k_B T) = x$, then find an expression for $\partial f(\mu)/\partial \mu$ and $\partial f(T)/\partial T$ in terms of $f(\varepsilon)$. By using the chain rule:

$$\frac{\partial f(\mu)}{\partial \mu} = \frac{\partial f}{\partial x} \frac{\partial x}{\partial \mu} = \frac{1}{k_B T} \frac{e^x}{(e^x + 1)^2} = -\frac{\partial f(\varepsilon)}{\partial \varepsilon} \quad (3.14)$$

$$\frac{\partial f(T)}{\partial T} = \frac{\partial f}{\partial x} \frac{\partial x}{\partial T} = \frac{\varepsilon - \mu}{k_B T^2} \frac{e^x}{k_B T (e^x + 1)^2} = \frac{\varepsilon - \mu}{T} \left(-\frac{\partial f(\varepsilon)}{\partial \varepsilon} \right) \quad (3.15)$$

Substituting $\partial f(\mu)/\partial \mu$ and $\partial f(T)/\partial T$ into Eq. 3.13:

$$\begin{aligned} f_L(\varepsilon) - f_R(\varepsilon) &= f(\varepsilon) + (\mu - \mu_L) \left(-\frac{\partial f(\varepsilon)}{\partial \varepsilon} \right) + (T - T_L) \frac{\varepsilon - \mu}{T} \left(-\frac{\partial f(\varepsilon)}{\partial \varepsilon} \right) \\ &\quad - \left[f(\varepsilon) + (\mu - \mu_R) \left(-\frac{\partial f(\varepsilon)}{\partial \varepsilon} \right) + (T - T_R) \frac{\varepsilon - \mu}{T} \left(-\frac{\partial f(\varepsilon)}{\partial \varepsilon} \right) \right] \\ &= (\mu_L - \mu_R) \frac{\partial f(\varepsilon)}{\partial \varepsilon} + (T_L - T_R) \frac{\varepsilon - \mu}{T} \frac{\partial f(\varepsilon)}{\partial \varepsilon} \end{aligned} \quad (3.16)$$

Then the current can be written as follows.

$$I = \frac{2e^2}{h} \int_{-\infty}^{+\infty} d\varepsilon \tau(\varepsilon) \Delta V \frac{\partial f(\varepsilon)}{\partial \varepsilon} - \frac{2e}{h} \int_{-\infty}^{+\infty} d\varepsilon \tau(\varepsilon) \Delta T \frac{\varepsilon - \mu}{T} \frac{\partial f(\varepsilon)}{\partial \varepsilon} \quad (3.17)$$

where $\mu_L - \mu_R = q\Delta V = -e\Delta V$ and $T_L - T_R = \Delta T$.

By recalling the Ohm's law ($V = IR$), one can define the conductance (which is the inverse of the resistance R) $G = I/V$. By using the current expression in Eq. 3.17 in which ΔT goes to zero, G is defined as:

$$G = \frac{2e^2}{h} \int_{-\infty}^{+\infty} d\varepsilon \tau(\varepsilon) \left(-\frac{\partial f(\varepsilon)}{\partial \varepsilon} \right), \quad (3.18)$$

which is known as Landauer's formula and the linear response of current to the applied bias can be deduced from this expression of conductance G .

3.2. Phononic Transport

Green's functions are being used to describe various phenomena in many branches of physics which includes the electronic (Meir and Wingreen, 1992) and phononic transport (Ozpineci and Ciraci, 2001; Mingo and Yang, 2003; Yamamoto and Watanabe, 2006). In phonon transport, the Green's function method is used for describing the heat current and for an expression for the transmission function obtained by Yamamoto and Watanabe (Yamamoto and Watanabe, 2006). Here, a brief information about retarded Green's functions are given for the equilibrium state (Sevinçli et al., 2019).

For the beginning, Hamiltonian is defined for obtaining the total energy of the system described with the atomic displacements from the equilibrium positions of the atoms. The mass-normalized displacements are defined as $u_{i,\alpha} = \sqrt{m_i} x_{i\alpha}$, where m_i is the mass of i^{th} atom and $x_{i\alpha}$ defines the displacements of i^{th} atom along the α -direction ($\alpha = x, y, z$).

$$H = \frac{1}{2} \sum_{i,\alpha} \dot{u}_{i,\alpha}^2 + \frac{1}{2} \sum_{ij,\alpha\beta} \phi_{ij,\alpha\beta} u_{i,\alpha} u_{j,\beta} + \dots + \frac{1}{3!} \sum_{ijk,\alpha\beta\gamma} \psi_{ijk,\alpha\beta\gamma} u_{i,\alpha} u_{j,\beta} u_{k,\gamma} \quad (3.19)$$

$$+ \frac{1}{4!} \sum_{ijkl,\alpha\beta\gamma\theta} \psi_{ijkl,\alpha\beta\gamma\theta} u_{i,\alpha} u_{j,\beta} u_{k,\gamma} u_{l,\theta},$$

where $\phi_{ij,\alpha\beta} = \partial^2 E_{tot} / (\partial u_{i\alpha} \partial u_{j\beta})$ are the dynamical matrix elements and, $\psi_{ijk,\alpha\beta\gamma} = \partial^3 E_{tot} / (\partial u_{i\alpha} \partial u_{j\beta} \partial u_{k\gamma})$ and $\psi_{ijkl,\alpha\beta\gamma\theta} = \partial^4 E_{tot} / (\partial u_{i\alpha} \partial u_{j\beta} \partial u_{k\gamma} \partial u_{l\theta})$ defines the anharmonic

force constants (which are mass-normalized). The second order terms are defined as the harmonic part of the Hamiltonian, H_{harm} , and the third and the higher order terms are included in the non-linear part (H_{int}). Harmonic part of the Hamiltonian is actually an eigenvalue problem.

$$\Phi|u_q\rangle = \omega^2|u_q\rangle, \quad (3.20)$$

where u_q and ω^2 are the eigenvectors and the corresponding eigenvalue, respectively and Φ is the dynamical matrix. Eq. 3.20 is the mass-normalized form of the eigenvalue problem. Without mass-normalization, it has a form as

$$V^{(2)}|x_q\rangle = \omega^2 M|x_q\rangle, \quad (3.21)$$

where the terms $V_{ij,\alpha\beta}^{(2)} = \partial E_{\text{tot}} / (\partial x_{i\alpha} \partial x_{j\beta})$ are the harmonic force constants and M represents the diagonal matrix of the atomic masses.

For the diagonalization of the $H_{\text{harm}} = \sum_q \hbar\omega (a_q^+ a_q + \frac{1}{2})$, one can use the annihilation and creation operators

$$a_q = \sqrt{\frac{\omega_q}{2\hbar}} (u_q + \frac{i}{\omega_q} \dot{u}_q) \quad (3.22)$$

$$a_q^+ = \sqrt{\frac{\omega_q}{2\hbar}} (u_q - \frac{i}{\omega_q} \dot{u}_q) \quad (3.23)$$

which satisfy the $[a_q, a_q^+] = \delta_{qq'}$.

Before defining the Green's function, it is necessary to remind that the left reservoir has a higher temperature and there is no scattering process inside the reservoirs. The sample part of the device is denoted as the central region (C) the connection between two reservoirs. All scattering events are included in this region. The related retarded Green's function is defined as

$$G^r(\omega) = [(\omega + i\delta)^2 \mathbb{I} - \Phi]^{-1}, \quad (3.24)$$

where δ is a positive number with an infinitesimal value and \mathbb{I} represents a unit matrix.

In the diagonal basis, the elements of the retarded Green's function can be defined as $G_{qq'}^r = \delta_{qq'} / (\omega^2 - \omega_q^2 + i\delta)$ with $\delta_{qq'}$ being the Kronecker- δ function.

The dynamical matrix and the retarded Green's function can be expressed in terms of matrices. Then the Eq. 3.24 becomes

$$\begin{aligned} & \begin{bmatrix} (\omega + i\delta)^2 \mathbb{I} - \Phi^{LL} & -\Phi^{LC} & 0 \\ -\Phi^{CL} & (\omega + i\delta)^2 \mathbb{I} - \Phi^{CC} & -\Phi^{CR} \\ 0 & \Phi^{RC} & (\omega + i\delta)^2 \mathbb{I} - \Phi^{RR} \end{bmatrix} \\ & \times \begin{bmatrix} G^{LL,r} & G^{LC,r} & G^{LR,r} \\ G^{CL,r} & G^{CC,r} & G^{CR,r} \\ G^{RL,r} & G^{RC,r} & G^{RR,r} \end{bmatrix} = \mathbb{I}. \end{aligned} \quad (3.25)$$

The second column of the product in Eq. 3.25 is the result of the following equations.

$$(g^{L,r})^{-1} G^{LC,r} - \Phi^{LC} G^{CC,r} = 0, \quad (3.26)$$

$$\Phi^{CL} G^{LC,r} + [(\omega + i\delta)^2 - \Phi^{CC,r}] G^{CC,r} - \Phi^{CR} G^{RC,r} = \mathbb{I}, \quad (3.27)$$

$$(g^{R,r})^{-1} G^{RR,r} - \Phi^{RC} G^{RC,r} = 0, \quad (3.28)$$

where the retarded Green's functions are defined as $g^{L/R,r} = [(\omega + i\delta)^2 \mathbb{I} - \Phi^{LL/RR}]^{-1}$ for uncoupled reservoirs. Green's function of the central region is attained by using the equations above.

$$G^{CC,r} = [(\omega + i\delta)^2 \mathbb{I} - \Phi^{CC} - \Sigma^{L,r} - \Sigma^{R,r}]^{-1} \quad (3.29)$$

where $\Sigma^{L/R} = \Phi^{CL/CR} g^{L/C} \Phi^{LC/RC}$ are the self energies caused by the coupling to the reservoirs.

By using the Green's function method, Rego and Kirczenow (Rego and Kir-

czenow, 1998) reproduced the Landauer-type formula for the heat current which is defined as follows.

$$J = \int_0^\infty \frac{d\omega}{2\pi} \hbar\omega [f_{BE}(\omega, T_L) - f_{BE}(\omega, T_R)] \tau(\omega) \quad (3.30)$$

where f_{BE} is the Bose-Einstein distribution function. $T_{L,R}$ and $\tau(\omega)$ are the temperature and frequency dependent transmission function, respectively.

3.3. Thermoelectric Properties

Thermoelectric materials convert heat to electrical energy. The efficiency of thermoelectric materials are given in terms of a dimensionless figure of merit which is defined as $ZT = (\sigma S^2 T) / \kappa$, where σ is the electrical conductivity and S represents the Seebeck coefficient, respectively. The total thermal conductivity, κ is inversely proportional to the ZT . The total thermal conductivity has contributions from the electron thermal conductivity, κ_e and the phonon thermal conductivity, κ_{ph} . From the definition of ZT , one can deduced that higher efficiency requires the higher electrical conductivity and the higher Seebeck coefficient and less the thermal conductivity.

- 1) **Conductance:** According to Ohm's law, in macroscopic scale, conductance of a conductor, G , is directly proportional to its conductivity, σ , and its cross-sectional area, A . The conductivity is an intrinsic property of the conductor. When the length of the conductor is reduced, the conductance is expected to increase indefinitely since G is inversely proportional to the length of the material. By definition, conductance is the ability to conduct electricity and it can be measured as:

$$G = - \left(\frac{I}{\Delta V} \right)_{\Delta T=0} \quad (3.31)$$

Conductance can also expressed in terms of transmission coefficient $\tau(E)$ using the total current derived is Landauer formalism.

$$\begin{aligned}
G &= -\frac{1}{\Delta V} \left(\frac{2e^2}{h} \int_{-\infty}^{+\infty} d\varepsilon \tau(\varepsilon) \Delta V \frac{\partial f(\varepsilon)}{\partial \varepsilon} - 0 \right) \\
&= \frac{2e^2}{h} \int_{-\infty}^{+\infty} d\varepsilon \tau(\varepsilon) \left(-\frac{\partial f(\varepsilon)}{\partial \varepsilon} \right) = e^2 L_0,
\end{aligned} \tag{3.32}$$

where

$$L_n = \frac{2}{h} \int_{-\infty}^{+\infty} d\varepsilon \tau(\varepsilon) \left(-\frac{\partial f(\varepsilon)}{\partial \varepsilon} \right) (\varepsilon - \mu)^n \tag{3.33}$$

- 2) **Seebeck Coefficient:** Seebeck coefficient gives the magnitude of conversion of heat to electrical power or vice versa. When a non-zero temperature gradient is applied to a device, there occurs a voltage between the two ends of the material. The ratio of the resulting voltage and the temperature difference is called the Seebeck coefficient whose absolute is known as the thermopower.

$$S = - \left(\frac{\Delta V}{\Delta T} \right)_{I=0} \tag{3.34}$$

For the derivation of the Seebeck coefficient in terms of transmission coefficient $\tau(E)$, one can start from making the total current in Landauer formalism equal to zero.

$$0 = \frac{2e^2}{h} \int_{-\infty}^{+\infty} d\varepsilon \tau(\varepsilon) \Delta V \frac{\partial f(\varepsilon)}{\partial \varepsilon} - \frac{2e}{h} \int_{-\infty}^{+\infty} d\varepsilon \tau(\varepsilon) \Delta T \frac{\varepsilon - \mu}{T} \frac{\partial f(\varepsilon)}{\partial \varepsilon} \tag{3.35}$$

or

$$\frac{2e^2}{h} \int_{-\infty}^{+\infty} d\varepsilon \tau(\varepsilon) \Delta V \frac{\partial f(\varepsilon)}{\partial \varepsilon} = \frac{2e}{h} \int_{-\infty}^{+\infty} d\varepsilon \tau(\varepsilon) \Delta T \frac{\varepsilon - \mu}{T} \frac{\partial f(\varepsilon)}{\partial \varepsilon} \tag{3.36}$$

By solving any of these equations for $-\Delta V/\Delta T$ the one can obtain S.

$$-\frac{\Delta V}{\Delta T} = -\frac{\frac{2}{h} \int_{-\infty}^{+\infty} d\varepsilon \tau(\varepsilon) \Delta T \frac{\varepsilon - \mu}{T} \frac{\partial f(\varepsilon)}{\partial \varepsilon}}{\frac{2}{h} \int_{-\infty}^{+\infty} d\varepsilon \tau(\varepsilon) \Delta V \frac{\partial f(\varepsilon)}{\partial \varepsilon}} = -\left(\frac{L_1}{eTL_0}\right) \quad (3.37)$$

3) Thermal Conductance of Electrons: Thermal conductivity is an intrinsic property of the material which measures the ability to conduct heat. It can be defined as the amount of heat which passes in unit time through a particular area and thickness when a temperature difference is applied between the two end of the material. Thermal current I_Q and thermal conductivity κ_{el} are defined as:

$$I_Q = \frac{2}{h} \int_{-\infty}^{+\infty} dE \tau(E) [f_L(E) - f_R(E)] (E - \mu) \quad (3.38)$$

$$\kappa_{el} = -\left(\frac{I_Q}{\Delta T}\right)_{I=0} \quad (3.39)$$

By equaling the heat current to zero and solving the equation for the applied bias:

$$\frac{2e^2}{h} \int_{-\infty}^{+\infty} d\varepsilon \tau(\varepsilon) \Delta V \frac{\partial f(\varepsilon)}{\partial \varepsilon} = \frac{2e}{h} \int_{-\infty}^{+\infty} d\varepsilon \tau(\varepsilon) \Delta T \frac{\varepsilon - \mu}{T} \frac{\partial f(\varepsilon)}{\partial \varepsilon} \quad (3.40)$$

$$e\Delta V \frac{2}{h} \int_{-\infty}^{+\infty} d\varepsilon \tau(\varepsilon) \frac{\partial f(\varepsilon)}{\partial \varepsilon} = \frac{\Delta T}{T} \frac{2}{h} \int_{-\infty}^{+\infty} d\varepsilon \tau(\varepsilon) (\varepsilon - \mu) \frac{\partial f(\varepsilon)}{\partial \varepsilon} \quad (3.41)$$

$$e\Delta V L_0 = \frac{\Delta T L_1}{T} \quad (3.42)$$

$$\Delta V = \frac{\Delta T}{eT} \frac{L_1}{L_0} \quad (3.43)$$

Using the resulting expression for ΔV in the heat current:

$$I_Q = \frac{2}{h} \int_{-\infty}^{+\infty} d\varepsilon \tau(\varepsilon) (\varepsilon - \mu) \left[-e\Delta V \frac{\partial f(\varepsilon)}{\partial \varepsilon} + \Delta T \frac{(\varepsilon - \mu)}{T} \frac{\partial f(\varepsilon)}{\partial \varepsilon} \right] \quad (3.44)$$

$$= -e\Delta V(-L_1) + \frac{\Delta T}{T}(-L_2) \quad (3.45)$$

$$= \frac{\Delta V L_1^2}{T L_0} - \frac{\Delta T}{T}(L_2) \quad (3.46)$$

Then thermal conductance of electrons can be written as:

$$\kappa_{el} = - \left(\frac{I_Q}{\Delta T} \right)_{I=0} = \frac{1}{T} \left(L_2 - \frac{L_1^2}{L_0} \right) \quad (3.47)$$

- 4) Lorenz Number:** Electrons carry charge and heat and there is a relation between their electrical and thermal conductivity investigated within the Wiedemann-Franz law. According to this law, the ratio of the thermal conductivity to the electrical conductivity in metals is directly proportional to a constant times temperature. This constant is called Lorenz number defined as $L = \kappa_{el}/(\sigma T)$ (Kittel, 1996). However, for semiconducting materials L fluctuates and it can have values between 0.2 and 10 (Esfarjani et al., 2006). Lorenz number takes an important role for the determination of the estimated value of phonon thermal conductivity experimentally (H.-S. Kim and Snyder, 2015).

Theoretical value of Lorenz number can be defined as:

$$L = \frac{\kappa_{el}}{GT} = \frac{1}{T^2} \left(L_2 - \frac{L_1^2}{L_0} \right) \frac{1}{e^2 L_0} = \frac{1}{e^2 T^2} \left(\frac{L_2}{L_0} - \frac{L_1^2}{L_0^2} \right) \quad (3.48)$$

The theoretical value of Lorenz number can be calculated analytically for a material whose chemical potential is set to zero. Considering the transport regime is ballistic, we calculated the theoretical value of Lorenz number for a simple metal and semiconductor. For a semiconductor with $\tau(E) = \Theta(E)$,

$$L_0 = \frac{2}{h} \int_0^{+\infty} d\varepsilon \left(-\frac{\partial f(\varepsilon)}{\partial \varepsilon} \right) = \frac{1}{h} \quad (3.49)$$

$$L_1 = \frac{2}{h} \int_0^{+\infty} d\varepsilon \left(-\frac{\partial f(\varepsilon)}{\partial \varepsilon} \right) \varepsilon = \frac{2}{h} k_B T \log(2) = \frac{2}{h} k_B T (0.69315) \quad (3.50)$$

$$L_2 = \frac{2}{h} \int_0^{+\infty} d\varepsilon \left(-\frac{\partial f(\varepsilon)}{\partial \varepsilon} \right) \varepsilon^2 = \frac{2}{h} (k_B T)^2 \frac{\pi^2}{6} \quad (3.51)$$

By using the L_n values in Eqs. 3.49- 3.51, Lorenz number is found to be $1.37(k_B/e)^2$ for a semiconductor at the band edges. For a simple metal, one can assume constant transmission probability, which leads L_1 integral is to be zero and the obtained value for Lorenz number is $(\pi^2/3)(k_B/e)^2$ (which is approximately $2.44 \times 10^{-8} W\Omega K^{-2}$). This result is exactly same as the Sommerfeld value of the Lorenz number which is also known as the degenerate limit (N. W. Ashcroft, 1975b).

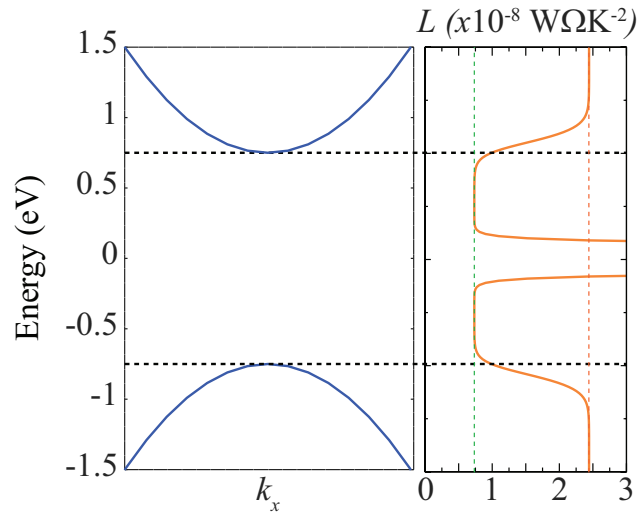


Figure 3.3. The band structure of a semiconductor is shown on the left. Fermi level is set to zero. In the right panel, Lorenz number L at 300 K of a semiconductor is given as a function of chemical potential. Red dashed lines represent the degenerate (Sommerfeld) limit which has a value of $2.44 \times 10^{-8} W\Omega K^{-2}$ and green dashed line is the lower limit with a value of approximately $0.75 \times 10^{-8} W\Omega K^{-2}$.

It was reported that L converges to the degenerate limit inside the bands; however, as approaching the band edges this value drops to $1.1 \times 10^{-8} W \Omega K^{-2}$ (H. Zhou, 2016b). By using the Eqs. 3.48- 3.51, we investigated the dependence of L on chemical potential μ and temperature. At 300 K, the relation between the L and μ is given in Fig. 3.3. As it is seen, L converges to the degenerate limit inside the bands and it is started drop as approaching to the band gap. Inside the band gap, L is approximately $0.75 \times 10^{-8} W \Omega K^{-2}$.

5) Thermal Conductance of Phonons: Phonons conduct heat in any case. Thermal conductance of phonons can be described as:

$$\kappa_p = \frac{1}{2\pi} \int_{-\infty}^{+\infty} d\omega \hbar \omega \tau(\omega) \frac{\partial f_{BE}(\omega, T)}{\partial T} \quad (3.52)$$

where f_{BE} is Bose-Einstein distribution function, $f_{BE} = 1/(\exp(\hbar\omega/k_B T) - 1)$ and $\tau(\omega)$ is the frequency dependent transmission function.

CHAPTER 4

STRUCTURAL, ELECTRONIC, VIBRATIONAL AND TRANSPORT PROPERTIES OF HfSe₂ STRUCTURES

In this study, the structural, electronic, vibrational and thermoelectric properties of T-HfSe₂ nanoribbons (NRs) having various widths are examined and the results are discussed. In the following sections, we discussed particular NRs in order to see the effect of nanostructuring on the properties of T-HfSe₂. The detailed information about the properties of all NRs and the computational methodology of our calculations are given in Appendix A.

4.1. Structural Properties

Top and side views of the relaxed single layer and NR geometries are shown in Fig. 4.1 and their calculated parameters are given in Table 4.1 The single layer HfSe₂ (SL-HfSe₂) is formed with the arrangement of three atomic sub-layers in the sequence of Se-Hf-Se. Here, the octahedral 1T phase of the SL-HfSe₂ which belongs to the $P\bar{3}m1(D3d)$ is investigated.

During the construction of the NRs, structures with zigzag and armchair edges are investigated. The structures with zigzag edges reveal metallic characteristics; thus, NR

Table 4.1. Calculated parameters of the single layer (SL-HfSe₂) and nanoribbon (NR) structures are; the lattice constant b ; the thickness of the structures, t ; the width of the structures; w , the energy band gaps calculated with PBE and PBE+HSE06 functionals, E_g^{PBE} and $E_g^{PBE+HSE06}$, respectively.

Structure	b (Å)	t (Å)	w (nm)	E_g^{PBE} (eV)	$E_g^{PBE+HSE06}$ (eV)
SL-HfSe ₂	3.76	3.14	-	0.60	1.50
n=13	6.54	3.26	2.30	0.66	1.35
n=12	6.54	3.26	2.12	0.72	1.41
n=7	6.53	3.27	1.18	0.67	1.37
n=6	6.60	3.25	0.99	0.98	2.01

structures with periodicity along the armchair direction are studied. Naming of NRs is based on the number of atoms, n , in the width of nanoribbon. As seen in Figs. 4.1(c) and (d), there is a difference between the arrangement in the edges of the structures with even and odd n . Considering the structures with odd n , both of edges are symmetric with respect to each other which means structures has the mirror image symmetry with a symmetry line passes through the center of the structures. This symmetry breaks down in the structures with even n and they reveal glide reflection symmetry. NRs are thicker than the SL-HfSe₂ and the change in the thickness is about 4%. When NRs are compared with the 2D counterpart, the bond lengths near the edges become shorter, but the average bond length in NR does not change drastically.

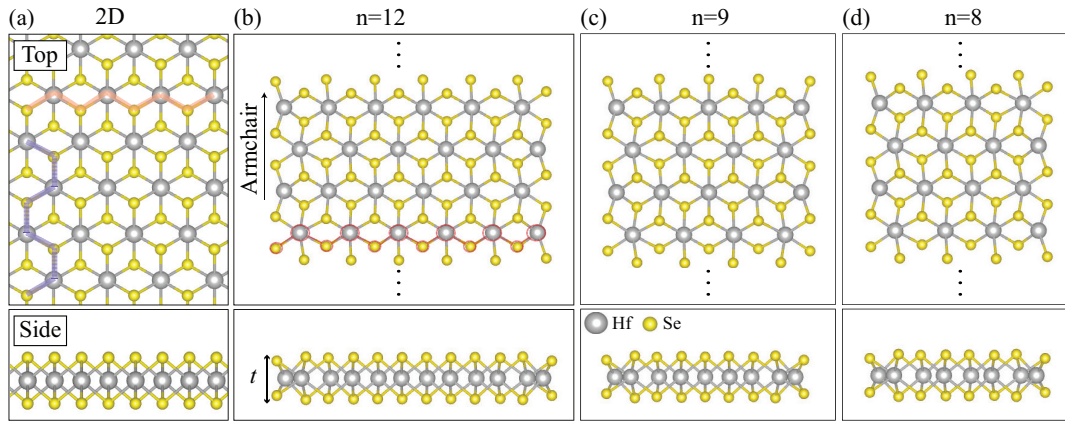


Figure 4.1. The geometries of the single layer (SL-HfSe₂) and nanoribbons (NRs) are represented. (a) Blue and orange lines show the armchair and zigzag directions, respectively. (b) Atoms marked with red circles define the number of atoms in the width of NR, n . In (c) and (d), NRs with two different type of edges are illustrated.

4.2. Electronic Properties

The calculated electronic band spectra of the structures are demonstrated in Fig. 4.2. According to our calculations, SL-HfSe₂ is a nonmagnetic semiconductor with energy gap calculated within PBE is 0.60 eV which is consistent with the literature (Özbal et al., 2019). As the dimension of the structure is reduced, the semiconducting character is preserved and the energy band gap increases. Reducing the number of chains one by one or in pairs effects the electronic band dispersion differently. As seen from the Figs. 4.2(b)-(e) the structures with odd (even) n reveals the same dispersion trend among them-

selves. This results from that structures with odd and even n have different symmetries as shown in Fig. 4.2(f).

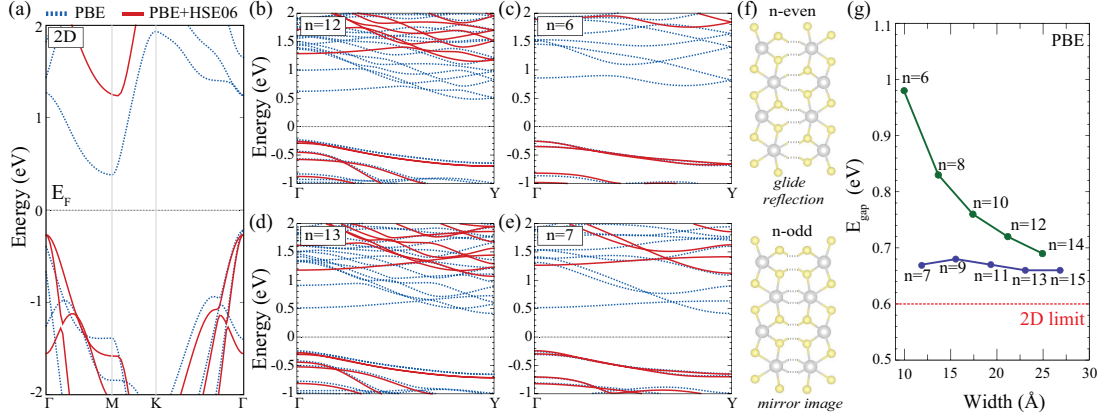


Figure 4.2. Electronic band structures for (a) single layer (SL-HfSe₂) and (b)-(e) nanoribbon (NR) structures with $n=6,7,12,13$ are presented. The Fermi level is set to zero. (f) NRs with even n have glide reflection symmetry, while NRs with odd n have mirror image symmetry. (g) As the width of the NR is getting wider, the energy band gap value converges to the band gap value of SL-HfSe₂.

As represented in Fig. 4.2, as the NR structure enlarges, the band gap of the NR converges to the band gap of the SL-HfSe₂. This is expected since the structure approaches to the 2D-limit. Moreover, the contributions come from the holes and the electrons cancels with each other when the energy band gap of the material is less than $10k_B T$ which results in suppression of the Seebeck coefficient (G. S. Nolas, 2001). In order to overcome this problem HSE06 hybrid functional is used for the band gap estimation.

4.3. Vibrational Properties

Here, the vibrational properties of SL-HfSe₂ and NR structures are examined. The calculated phonon spectra of the structures are shown in Fig. 4.3. The vibrational analyses reveal that each structure has non-negative phonon branches through the whole BZ. This indicates the dynamical stability of the structures at $T = 0$ K.

Maximum frequency of the optical phonon branch for 2D structure is less than 250 cm^{-1} . When the dimension is reduced, this value increases over 250 cm^{-1} and does not differ with the width of the NR structures. Since Hf and Se atoms are relatively

massive and the bonds in the material is weak, the maximum value of the frequency has value about 250 cm^{-1} .

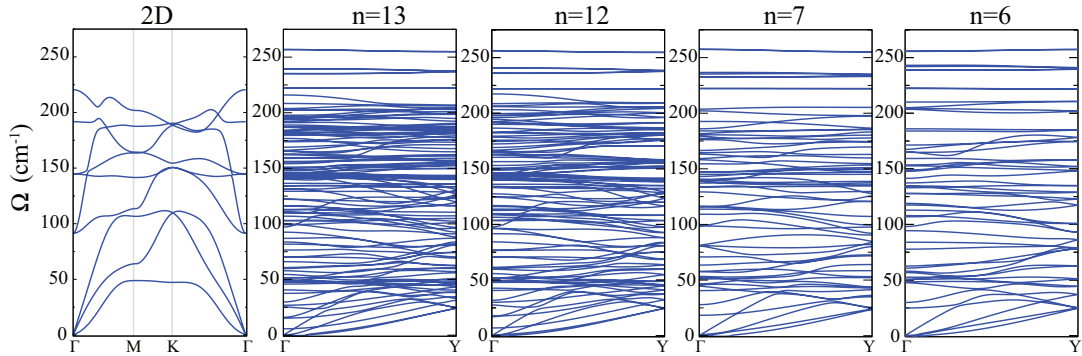


Figure 4.3. Phonon band spectra of the single layer (SL-HfSe₂) and nanoribbon (NRs) structures are presented.

For each structure, there are $3N$ number of phonon branches where N is the number of atoms in the unit cell. Decrease in the number of branches can be seen in Fig. 4.3 with the decreasing of N . In 2D structures, there are 3 acoustic and $3N-3$ optical phonon branches. When dimension is reduced to 1D, the number of acoustic phonon branches increase up to four since a rotational motion that costs zero energy is participated and the motion reveals itself as acoustic vibration.

Moreover, the optical phonon mode with the lowest energy has an in-plane characteristics. As it seen from Figs. 4.3, the frequencies of these mode increase as the structure is getting narrower. Thus, these modes are essential for the determination of the widths of the NR structures.

4.4. Thermoelectric Properties

In this section, thermoelectric properties of the single layer and NR structures; and particularly, the width dependency of the thermoelectric figure of merit ZT are discussed. The calculated values of these thermoelectric coefficients such as the Seebeck coefficient S , the power factor P and the ZT at various temperatures are given in Table. 4.2. The given ZT values are the maximum values (near the conduction and valance band edges), and the Seebeck coefficient and the power factor values correspond to the chemical potentials at which ZT peaks.

For the NR structure with $n=12$, ZT and the phonon thermal conductance per

Table 4.2. The calculated parameters of the single layer (SL-HfSe₂) (Özbal et al., 2019) and nanoribbon structures are; p- and n-type Seebeck coefficient, S ; power factor, P , thermoelectric figure of merit, ZT , and phonon thermal conductance per nm, κ_p .

Structure	S ($10^{-4}V/K$)		P ($10^{-3}nW/K^2nm^2$)		ZT	
	300 K	800 K	300 K	800 K	300 K	800 K
SL-HfSe ₂	1.92 / -2.20	2.12 / -2.65	0.56 / 1.84	0.92 / 2.61	0.26 / 0.75	0.84 / 2.11
n=13	2.35 / -2.36	2.47 / -2.63	1.40 / 1.08	1.78 / 2.25	0.89 / 0.62	1.96 / 2.16
n=12	2.39 / -2.15	2.49 / -2.65	1.32 / 1.48	1.66 / 1.96	0.83 / 0.95	1.97 / 2.11
n=7	2.37 / -2.22	2.55 / -2.45	1.12 / 0.82	1.37 / 1.13	1.08 / 0.85	2.57 / 2.09
n=6	2.25 / -2.45	2.72 / -2.68	0.83 / 1.47	1.24 / 1.38	0.94 / 1.55	2.62 / 3.12

width are shown as a function of temperature and ZT is also given as a function of chemical potential in Fig. 4.4. At the temperatures above 300 K, ZT reveals increasing performance. This results partly from that the phonon thermal conductance is constant for those temperature values since the maximum frequency remains at 250 cm^{-1} (see Fig. 4.3). ZT decreases with increasing the phonon thermal conductance; thus, the main contribution to total κ comes from the electronic part and the thermoelectric efficiency increases almost linearly. As seen in Fig. 4.4, for the temperatures above 900 K, ZT values start to decrease with the increasing temperature because $10k_B T$ limit is reached. Therefore, n-type and p-type contributions start to cancel each other which results in a decrease in ZT value.

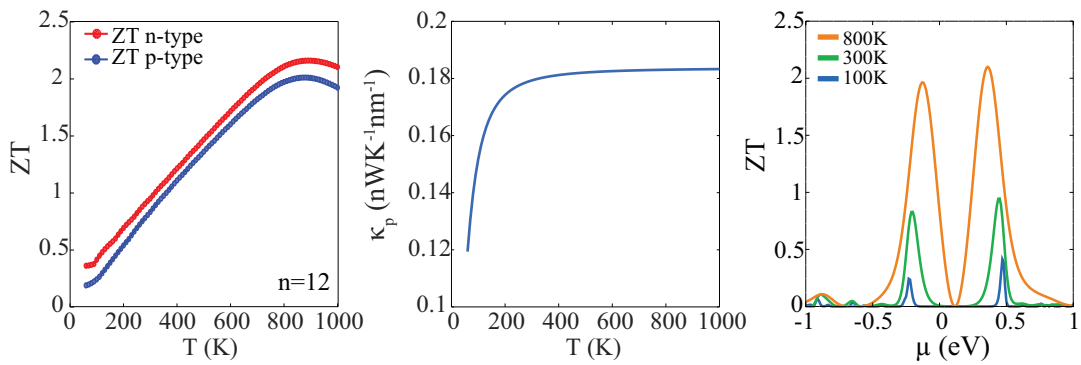


Figure 4.4. From left to right, thermoelectric figure of merit (ZT) as a function of temperature, the phonon thermal conductance (κ_p) and ZT as a function of chemical potential (μ) are given for nanoribbon (NR) with $n=12$.

The temperature and width dependencies of ZT are investigated and they are shown in Fig. 4.5. When the dimension of the structure is reduced, p-type Seebeck co-

efficient and power factor values increase. At both low and high temperatures, p-type ZT values of NRs with odd and even n are enhanced. At low temperatures, n-type ZT shows the same trend as p-type. As the width of the NR enlarges, the ZT values of NRs converge to the 2D limit.

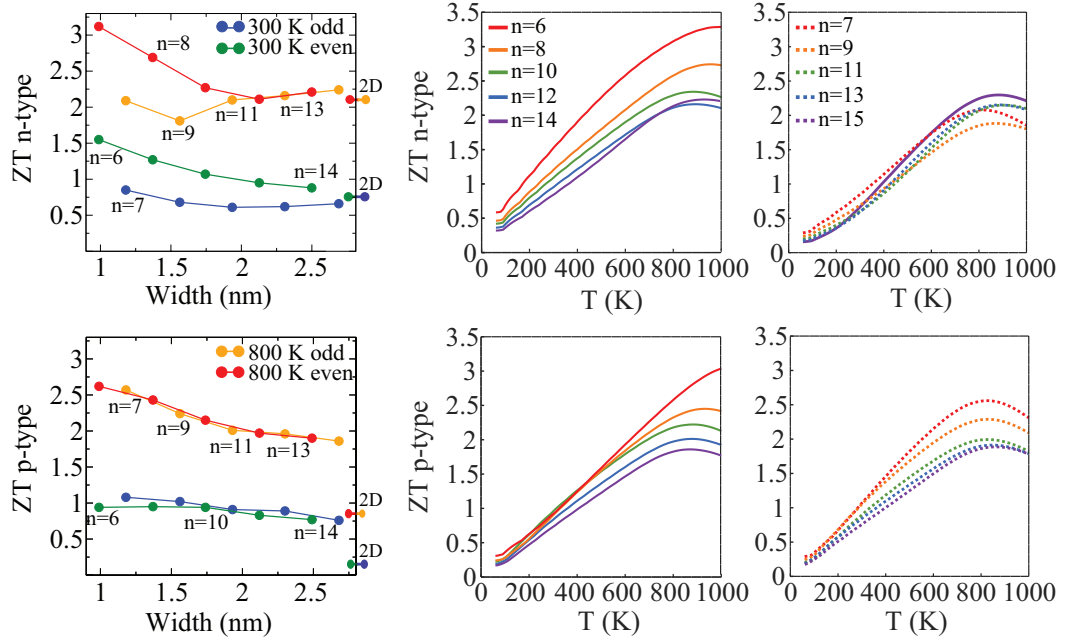


Figure 4.5. In the top panel, variation of n-type thermoelectric figure of merit (ZT) with the width of the nanoribbon (NR) and ZT as function of temperature for NRs with even and odd n are given. p-type ZT values are given in the bottom panel.

ZT value is expected to decrease as the width of the structure increases. As seen in Fig. 4.5, n-type ZT values of structures with odd n at 800 K show a different trend from the expected. In order to understand this behaviour in ZT -width relation, the electronic band and their transmission spectra are investigated in detail. Their band dispersion and transmissions; and at various temperatures, the power factor and ZT graphs are shown in Fig. 4.6. ZT of the structure with $n=11$ and $n=13$ have higher values than that of the narrower ones. As seen in Fig. 4.6, as n increases, first conduction plateau of the transmission spectrum of the structures is getting narrower due the band degeneracy in their electronic band structure. This results in having two peaks with similar values in their power factor values. At low temperatures, these two peaks are separated from each other. As the temperature increases, these peaks interfere with each other constructively and this causes an increase in n-type ZT values of the NRs with $n=11$ and $n=13$. Moreover, increase in the number of electronic band leads an increase in transmission. This also

makes contribution to the increment of ZT values.

The width and temperature dependence of phonon thermal conductance κ_p is investigated. The calculated κ_p values for 300 and 800 K are given in Fig. 4.7. κ_p is also given as a function of temperature in Fig. 4.7. The given values are scaled with respect to the width of the NRs. The κ_p of SL-HfSe₂ along zigzag and armchair directions are isotropic and they are scaled with respect to the width of the unit cell (Özbal et al., 2019).

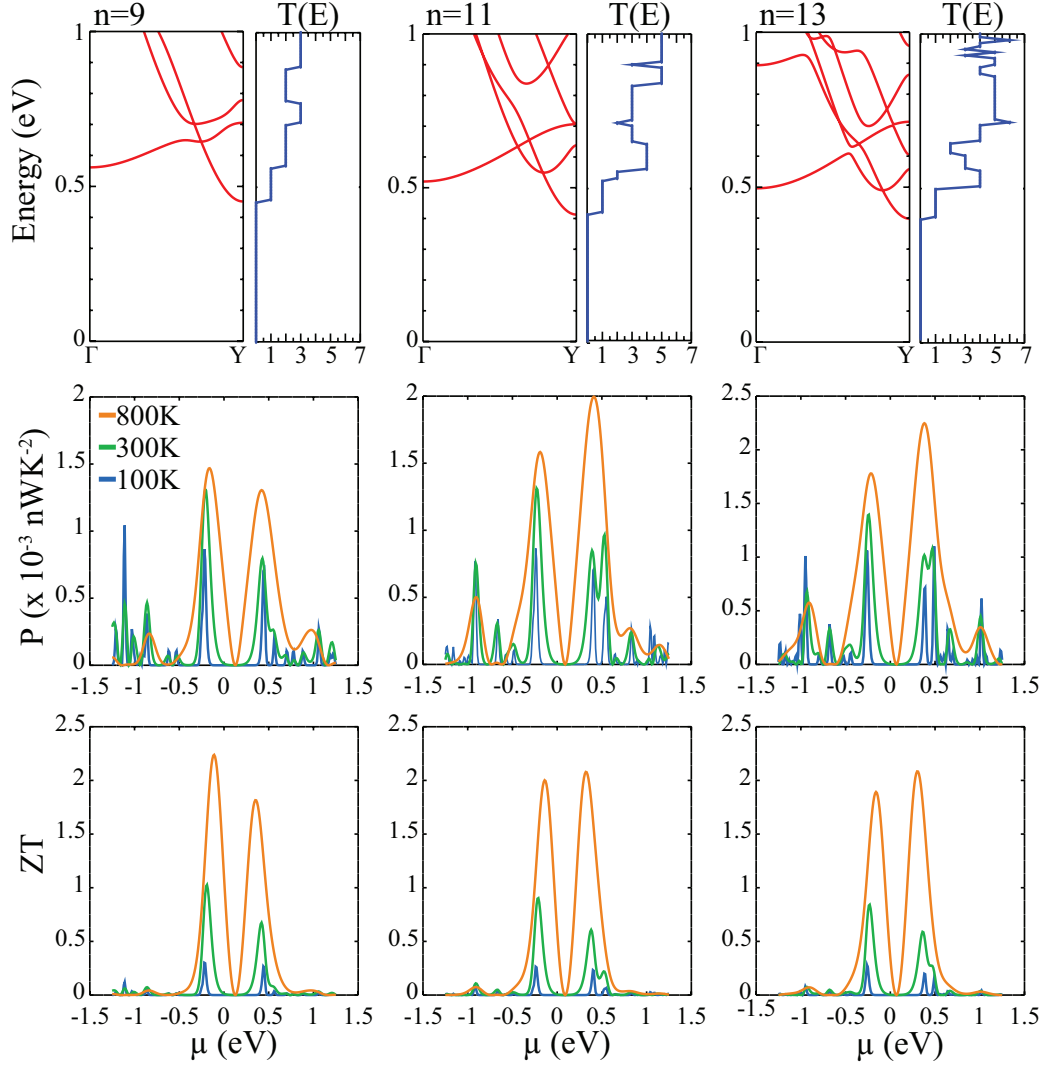


Figure 4.6. For the nanoribbons (NRs) with $n=9$, $n=11$ and $n=13$, the electronic band and their transmission spectra are given in the first row. Power factor and thermoelectric figure of merit (ZT) are shown in the second and third rows, respectively.

As seen in Fig. 4.7, the calculated κ_p values at 300 and 800 K are close to each other. As the width of the structure decreases, κ_p values increase. The lattice thermal conductance and the width do not change with the same rate. In order to see the convergence

of κ_p to 2D limit, one can construct NRs with widths larger than 2.68 nm; however, this increases the computational cost. Therefore, NR structures larger than 2.68 nm are not considered in this study.

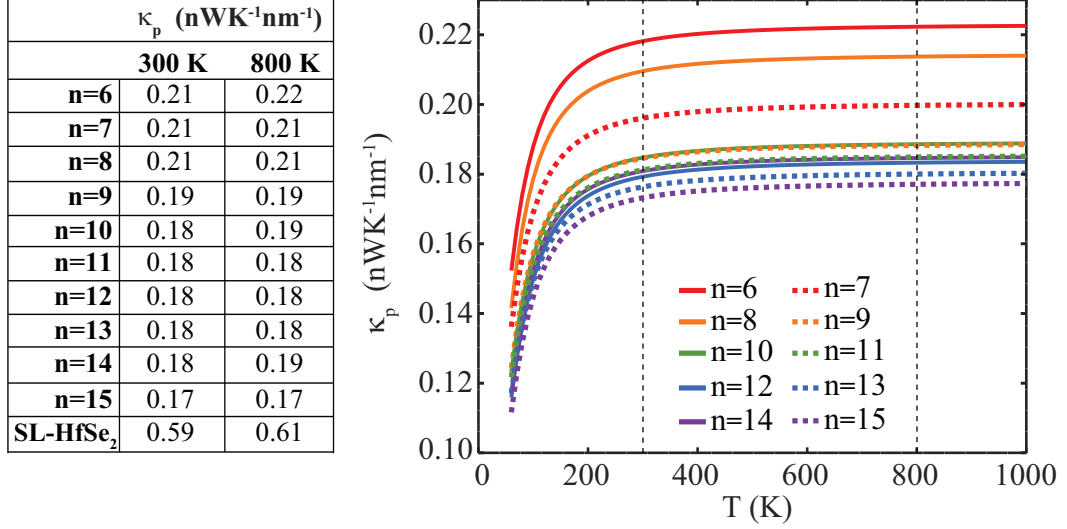


Figure 4.7. In the left panel, the phonon thermal conductance (κ_p) of the single layer T-HfSe₂ (SL-HfSe₂) and nanoribbon (NR) structures are given at 300 and 800K. In the right panel, κ_p of NR structures are given as a function of temperature. κ_p values are the scaled values with respect to the width of the NRs. κ_p values of SL-HfSe₂ are from the study of Özbal et al. (2019).

Furthermore, Lorenz number of the NRs are calculated at 300 K and the calculated values are close to the degenerate semiconductor (Sommerfeld) limit. The scaled values of L (with respect to Sommerfeld value) are given in Appendix A. The chemical potential of a material can be tuned by doping or applying a gate voltage and the chemical potential dependency of Lorenz number is a study topic in literature (H. Zhou, 2016a). Therefore we calculated L values of NRs given as a function of chemical potential given in Fig. 4.8. The L values where the chemical potential within the conduction and valence bands converge to the degenerate limit. When the chemical potential inside the band gap, the proportionality is altered since there is no carrier in that energy range (H. Zhou, 2016b).

As it is seen in Fig. 4.8, near the conduction and valence band edges, L is higher than the theoretical value ($0.75 \times 10^{-8} W \Omega K^{-2}$) mentioned in Ch. 3. Inside the bands, L value fluctuates around Sommerfeld value for each NR structure and the fluctuations result from the change in the transmission function (given in Appendix A).

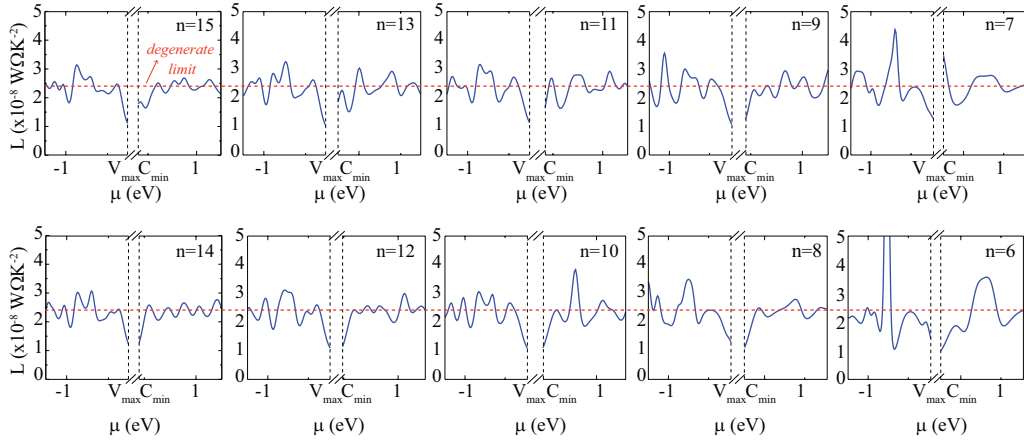


Figure 4.8. Lorenz number L of the nanoribbons (NRs) is given as a function of chemical potential μ at 300 K. Red dashed lines represent the degenerate (Sommerfeld) limit which has a value of $2.44 \times 10^{-8} W\Omega K^{-2}$. V_{max} and C_{min} are the valence band maximum and conduction band minimum values, respectively.

In literature, the deviations from the theoretical value of Lorenz number is an object at issue. It was reported that using a constant value for L is not convenient in cases where there is not enough information about the band structure and the scattering mechanism. For the degenerate limit, it was suggested a correction which depends on the thermopower. It was also mentioned that the deviations are caused by multiple band behaviour in thermopower-dependent Lorenz number (H.-S. Kim and Snyder, 2015).

CHAPTER 5

CONCLUSIONS

In the beginning of this thesis, we mentioned the 2D materials, particularly, TMDs and several structural and electronic properties of TMDs that make them relevant about thermoelectricity. Moreover, a brief information about the thermoelectric materials and their working principles were given and discussed how to enhance their thermoelectric efficiencies.

Here, we investigated the enhancement in ZT values of 2D T-HfSe₂. As mentioned before, the nanostructuring is one of the effective methods in that manner. Therefore, we generated NR structures with various widths and investigated their electronic and phononic band structures via density functional theory-based first-principles calculations. The quasi-one dimensional T-phase HfSe₂ structures were found to be dynamically stable at zero Kelvin and analyzed how their electronic band structure varies with their widths.

In this study, our main focus was to enhance the thermoelectric properties of the T-phase HfSe₂ structures via nanostructuring. We investigated the ballistic transport properties within the Landauer formalism. In conclusion, we calculated that the p-type ZT parameter of T-phase HfSe₂ at both low and high temperatures are enhanced. Moreover, thermoelectric properties of the NR with different width are compared with each other and as a result, we found that the thermoelectric properties HfSe₂ is enhanced forming its quasi-one dimensional structures as predicted. Beside reducing the dimensions, we found that the effect of band degeneracy has also contribution to the ZT increment. We reported that NR structures of T-phase HfSe₂ are suitable candidates in thermoelectric device applications.

REFERENCES

- A. V. Krukau, O. A. Vydrov, A. F. I. G. E. S. (2006). Influence of the exchange screening parameter on the performance of screened hybrid functionals. *J. Chem. Phys.* 125.
- Balandin, A. (2011). Thermal properties of graphene and nanostructured carbon materials. *Nature Mater* 10, 569–581.
- Born, M. and R. Oppenheimer (1927). Zur quantentheorie der molekeln. *Annalen der Physik* 389(20), 457–484.
- Brocks, G. (2005). Electron transport at the nanoscale lecture notes, preliminary version.
- Büttiker, M. (1986, Oct). Four-terminal phase-coherent conductance. *Phys. Rev. Lett.* 57, 1761–1764.
- Castellanos-Gomez A, Poot M, S. G. v. d. Z. H. A. N. R.-B. G. (2012). Elastic properties of freely suspended mos2 nanosheets. *Adv. Mater.* 24, 772–775.
- D. K. Ferry, S. M. Goodnick, J. B. (2009). *Transport in Nanostructures*. Cambridge University Press.
- Datta, S. (2004, may). Electrical resistance: an atomistic view. *Nanotechnology* 15(7), S433–S451.
- Datta, S. (2009). *Electronic Transport in Mesoscopic Systems*. Cambridge University Press.
- Dirac, P. A. M. (1930). Note on exchange phenomena in the thomas-fermi atom. *Proc. Cambridge Phil. Roy. Soc.* 26, 376–385.
- Esfarjani, K., M. Zebarjadi, and Y. Kawazoe (2006, Feb). Thermoelectric properties of a nanocontact made of two-capped single-wall carbon nanotubes calculated within the tight-binding approximation. *Phys. Rev. B* 73, 085406.
- Ewald, P. (1921). Die berechnung optischer und elektrostatischer gitterpotentiale.

Annalen der Physik 369(3), 253–287.

Fermi, E. (1927). Un metodo statistico per la determinazione di alcune priorieta dell'atome. *Rend. Accad. Naz. Lincei* 6, 602–607.

Fock, V. (1930). A method for the solution of many-body problems in quantum mechanics. *Zeitschrift for Physik* 61, 126–148.

Franz, R.; Wiedemann, G. (1853). Ueber die warme-leitungsfahigkeit der metalle. *Annalen der Physik (in German)* 165, 497–53.

G. J. Snyder, E. S. T. (2008). Complex thermoelectric materials. *Nat. Mater.* 7, 105–114.

G. S. Nolas, J. Sharp, H. J. G. (2001). *Thermoelectrics: Basic Principles and New Materials Developments*. Springer.

H. Alam, S. R. (2013). A review on the enhancement of figure of merit from bulk to nano-thermoelectric materials. *Nano Energy* 2, 190–212.

H.-S. Kim, Z. M. Gibbs, Y. T. H. W. and G. J. Snyder (2015). Characterization of lorenz number with seebeck coefficient measurement. *APL materials* 3, 041506.

H. Zhou, Y. Cai, G. Z. Y.-W. Z. (2016a). Quantum thermal transport in stanene. *Phys. Rev. B* 94, 045423.

H. Zhou, Y. Cai, G. Z. Y.-W. Z. (2016b). Thermoelectric properties of phosphorene at the nanoscale. *Journal of Materials Research* 31, 3179–3186.

Hartree, V. F. R. (1928). The wave mechanics of an atom with a non-magnetic coulomb central field. *Proceedings of the Cambridge Philosophical Society* 24, 89–132.

Hicks, L. D. and M. S. Dresselhaus (1993a, May). Effect of quantum-well structures on the thermoelectric figure of merit. *Phys. Rev. B* 47, 12727–12731.

Hicks, L. D. and M. S. Dresselhaus (1993b, Jun). Thermoelectric figure of merit of a one-dimensional conductor. *Phys. Rev. B* 47, 16631–16634.

- Hohenberg, P. and W. Kohn (1964, Nov). Inhomogeneous electron gas. *Phys. Rev. 136(3B)*, 864–871.
- Huang, Pu, H. C. J. C. C. I. T. L. (2014). Large-area synthesis of highly crystalline wse₂ monolayers and device applications. *ACS Nano* 8, 923–930.
- J. Heyd, G. E. Scuseria, M. E. (2003). Hybrid functionals based on a screened coulomb potential. *J. Chem. Phys.* 118.
- Kittel, C. (1996). *Introduction to Solid State Physics*. Wiley.
- Kong, Wang, C. P. K. Y. C. (2013). Synthesis of mos₂ and mose₂ films with vertically aligned layers. *Nano Lett.* 13, 1341–1347.
- Kresse, G. and J. Furthmüller (1996, Oct). Efficient iterative schemes for ab initio total-energy calculations using a plane-wave basis set. *Phys. Rev. B* 54, 11169–11186.
- Kresse, G. and J. Hafner (1993, Jan). Ab initio molecular dynamics for liquid metals. *Phys. Rev. B* 47, 558–561.
- L. E. F. F. Torres, S. Roche, J.-C. C. (2014). *Introduction to Graphene-Based Nanomaterials: From Electronic Structure to Quantum Transport*. Cambridge University Press.
- Landauer, R. (1957). Spatial variation of currents and fields due to localized scatterers in metallic conduction. *IBM Journal of Research and Development* 1, 223–231.
- Landauer, R. (1970). Electrical resistance of disordered one-dimensional lattices. *The Philosophical Magazine: A Journal of Theoretical Experimental and Applied Physics* 21(172), 863–867.
- Mak, Lee, H. S. H. (2010). Atomically thin mos₂: a new direct-gap semiconductor. *Phys. Rev. Lett.* 105.
- Mao, J., H. Z. Z. D. Z. L.-G. A. G. G. C. and Z. Ren (2019). Highthermoelectric cooling performance of n-type mg₃bi₂-based materials. *Science* 365, 495–498.

- Martin, R. M. (2004). *Electronic Structure: Basic Theory and Practical Methods*. Cambridge University Press.
- Meir, Y. and N. S. Wingreen (1992, Apr). Landauer formula for the current through an interacting electron region. *Phys. Rev. Lett.* 68, 2512–2515.
- Mingo, N. and L. Yang (2003, Dec). Phonon transport in nanowires coated with an amorphous material: An atomistic green's function approach. *Phys. Rev. B* 68, 245406.
- Mleczko, Zhang, L. K. M.-K. M. S.-F. N. and Pop (2017). Hfse2 and zrse2: Two-dimensional semiconductors with native high-kappa oxides. *Sci. Adv.* 3 (8).
- N. W. Ashcroft, N. D. M. (1975a). *Solid State Physics*. Saunders College Publishing.
- N. W. Ashcroft, N. D. M. (1975b). *Solid State Physics*. Saunders College Publishing.
- Novoselov, Geim, M. J. Z. D. G. F. (2004). Electric field effect in atomically thin carbon films. *Science* 306, 666–9.
- Özbal, G., R. T. Senger, C. Sevik, and H. Sevinçli (2019, Aug). Ballistic thermoelectric properties of monolayer semiconducting transition metal dichalcogenides and oxides. *Phys. Rev. B* 100, 085415.
- Ozpineci, A. and S. Ciraci (2001, Mar). Quantum effects of thermal conductance through atomic chains. *Phys. Rev. B* 63, 125415.
- Perdew, J. P., K. Burke, and M. Ernzerhof (1996, Oct). Generalized gradient approximation made simple. *Phys. Rev. Lett.* 77, 3865–3868.
- Poudel, B., Q. H. Y. M. Y. L.-A. M. B. Y. X. Y.-D. W. A. M. D. V. X. C. J. L. M. S. D. G. C. and Z. Ren (2008). High-thermoelectric performance of nanostructured bismuth antimony telluride bulk alloys. *Science* 320, 634–638.
- Rego, L. G. C. and G. Kirczenow (1998, Jul). Quantized thermal conductance of dielectric quantum wires. *Phys. Rev. Lett.* 81, 232–235.
- Sahoo, S., A. P. S. Gaur, M. Ahmadi, M. J.-F. Guinel, and R. S. Katiyar (2013).

Temperature-dependent raman studies and thermal conductivity of few-layer mos₂. *The Journal of Physical Chemistry C* 117(17), 9042–9047.

Sevinçli, H., S. Roche, G. Cuniberti, M. Brandbyge, R. Gutierrez, and L. M. Sandonas (2019, apr). Green function, quasi-classical langevin and kubo–greenwood methods in quantum thermal transport. *Journal of Physics: Condensed Matter* 31(27), 273003.

Toffoli, H. (2012, Nov). *PHYS 741 Lecture Notes*.

Togo, A. and I. Tanaka (2015, Nov). First principles phonon calculations in materials science. *Scr. Mater.* 108, 1–5.

Velusamy DB, Kim RH, C. S. H. J.-K. R. K. S. S. G.-C. S. C. S. H. I. L. J. O. K. C. H. P. C. (2015). Flexible transition metal dichalcogenide nanosheets for band-selective photodetection. *Nat. Commun.* 6, 8063.

W. Kohn, L. J. S. (1965). Self-consistent equations including exchange and correlation effects. *Physical Review* 140, A1133–A1138.

Wang, Kalantar-Zadeh, K. C. S. (2012). Electronics and optoelectronics of two-dimensional transition metal dichalcogenides. *Nat. Nanotechnol.* 7, 699–712.

Xiao, Y. and L.-D. Zhao (2018). Charge and phonon transport in pbte-based thermoelectric materials. *npj Quantum Materials* 3.

Y. Imry, R. L. (1999, Mar). Conductance viewed as transmission. *Rev. Mod. Phys.* 71, S306–S312.

Yamamoto, T. and K. Watanabe (2006, Jun). Nonequilibrium green's function approach to phonon transport in defective carbon nanotubes. *Phys. Rev. Lett.* 96, 255503.

Yu, Li, Z. and Chang (2015). Synthesis of high quality two-dimensional materials via chemical vapor deposition. *Chem. Sci.* 6, 6605–6716.

Zhang, Sun, L. L. C. C. Y. H.-H. (2015). Measurement of lateral and interfacial thermal conductivity of single- and bilayer mos₂ and mose₂ using refined optothermal raman technique. *ACS Appl Mater Interfaces.* 7, 25923–25929.

Zhang, Yao, S. Y. Z. W. W. and He (2019). Recent progress in cvd growth of 2d transition metal dichalcogenides and related heterostructures. *Adv. Mater.* 31 (41).

APPENDIX A

NANORIBBON STRUCTURES OF T-HfSe₂

In this study, we constructed ten different nanoribbons (NRs) and their widths vary between $n = 6$ to $n = 15$. In this part, detailed information about structural, electronic, vibrational and thermoelectric properties of each NR are given. Computational details are also given in this part.

A.1. Structural Properties

The geometrical optimization is performed by adopting Perdew-Burke-Ernzerhof (PBE) form of the generalized gradient approximation (GGA) functional for describing the exchange-correlation energies. The cutoff energy of the plane-wave basis set was taken to be 250 eV. For the convergence criterion, the energy difference between successive electronic steps was chosen to be 10^{-5} eV and the Hellmann-Feynman forces on each atom were reduced to a value of less than 10^{-4} eV/Å. For the Brillouin Zone integration of the unit cell, we used $1 \times 12 \times 1$ Γ -centered mesh. The NR structures are assumed to

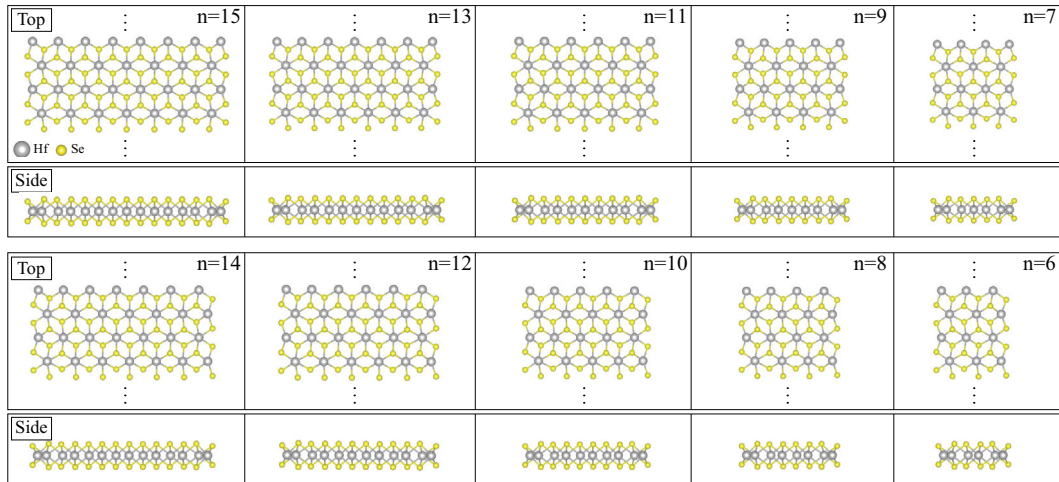


Figure A.1. The optimized geometries of the nanoribbon (NR) structures with odd n (upper row) and even n (lower row) are given. Grey and yellow atoms represents the Hf and Se atoms, respectively.

Table A.1. Calculated parameters of the single layer (SL-HfSe₂) and nanoribbon (NR) structures with various n are; the lattice constant b ; the thickness of the structures, t ; the width of the structures; w , the energy band gaps calculated with PBE and PBE+HSE06 functionals, E_g^{PBE} and $E_g^{PBE+HSE06}$, respectively.

Structure	b (Å)	t (Å)	w (nm)	E_g^{PBE} (eV)	$E_g^{PBE+HSE06}$ (eV)
SL-HfSe ₂	3.76	3.14	-	0.60	1.50
n=15	6.53	3.26	2.68	0.66	1.34
n=14	6.54	3.26	2.49	0.69	1.38
n=13	6.54	3.26	2.30	0.66	1.35
n=12	6.54	3.26	2.12	0.72	1.41
n=11	6.54	3.26	1.93	0.67	1.36
n=10	6.55	3.26	1.74	0.76	1.46
n=9	6.54	3.26	1.56	0.68	1.37
n=8	6.57	3.26	1.37	0.83	1.54
n=7	6.53	3.27	1.18	0.67	1.37
n=6	6.60	3.25	0.99	0.98	2.01

be periodic in the y-direction; therefore, at least 12 Å of vacuum space is used for the confined directions (x- and z-directions). Top and side views of relaxed geometries of each NR are shown in Fig. A.1. Their calculated structural and electronic parameters are given in Table A.1.

A.2. Electronic Properties

The electronic band dispersions of each NR are calculated within the PBE and HSE06 hybrid functional was adopted for the band gap estimation. For the electronic band structure calculations, we used the same convergence criteria as used in geometrical optimization. Transmission spectrum is calculated by counting the number of bands (channels) in the corresponding energy range.

The calculated band diagrams and the edge symmetries of the two different type of armchair NRs are given in Fig. A.2. Different trend in the electronic band dispersion of the structures with odd and even n can be seen from the Fig. A.2. For the each structure, the electronic band structures and transmissions calculated within PBE are also given. The band degeneracy and the transmission increase as the width of the structure enlarges.

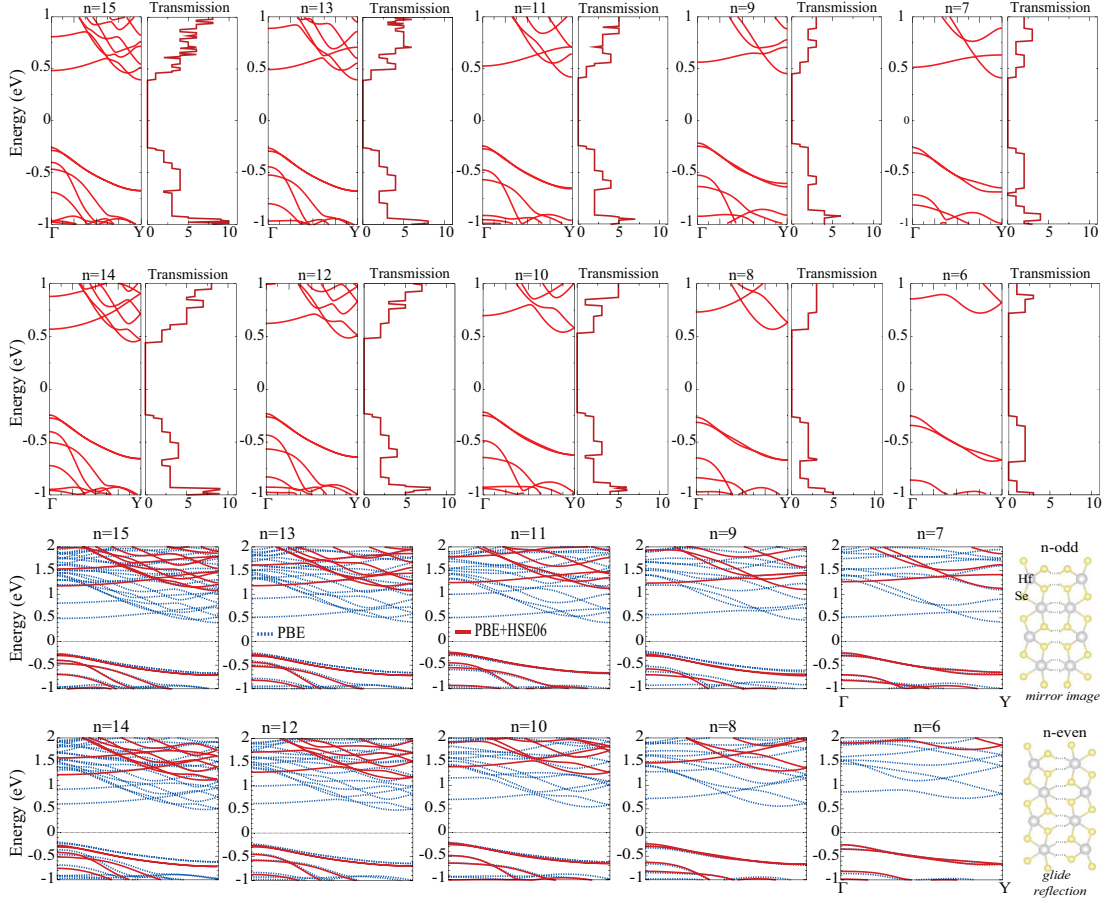


Figure A.2. The electronic band structures and transmissions calculated within PBE are given for the nanoribbon (NR) structures with odd n (first row) and even n (second row). The electronic band structures of NRs with odd n (third row) and even n (fourth row) calculated within PBE and PBE+HSE06 are shown. The symmetry of the structures are also given. grey and yellow atoms represent the Hf and Se atoms, respectively.

A.3. Vibrational Properties

For the phonon band spectrum calculations, the convergence criteria were not changed. For the Brillouin Zone integration, $1 \times 10 \times 1$ Γ -centered mesh was used. The vibrational properties of NRs were investigated for $1 \times 6 \times 1$ supercell by using the small displacement method as implemented in Phonopy code (Togo and Tanaka, 2015). Transmission spectrum gives the number of modes in the corresponding frequency range.

For the structures with $n = 15$ and $n = 14$, negative frequency occurs around Γ high symmetry point caused by numerical error. The structures with $n = 15$ and $n = 14$ include relatively more atoms within their unitcells. Therefore, for these structures, $1 \times 5 \times 1$

supercell and $1 \times 6 \times 1$ Γ -centered mesh were used for the phononic band calculations.

The calculated phononic band spectra and their transmission functions are given in Fig. A.3 and as it is seen, each nanoribbon structure is found to be dynamically stable. The number of atoms in the unit cell increases with the width of the NR; thus, the number of phonon branches and the transmissions increase.

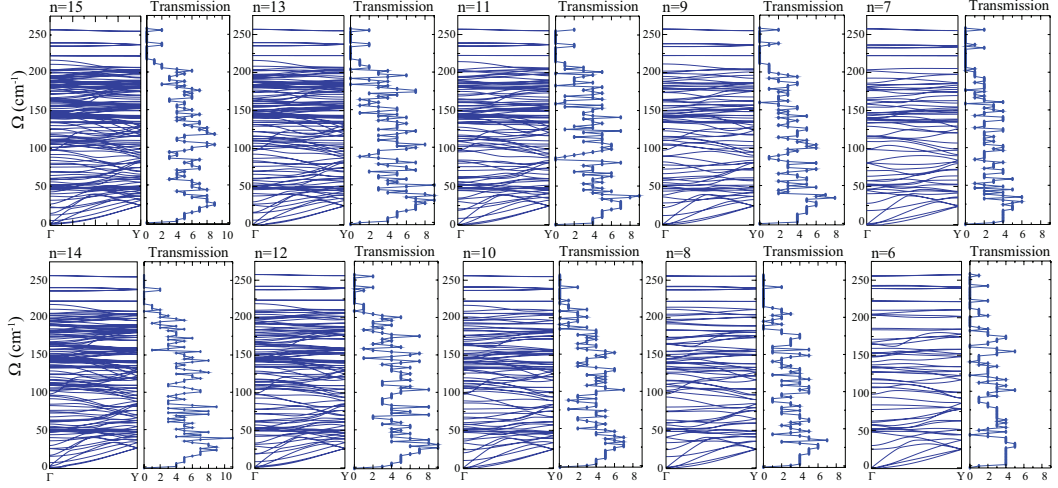


Figure A.3. The vibrational spectra and their transmissions for the nanoribbon (NR) structures with odd (upper row) and even (lower row) n are given.

A.4. Thermoelectric Properties

In order to compute the thermoelectric properties, we calculated the L_n integral in Eq. 3.33 for $n = 0, 1, 2$ and we used the definitions of electrical conductance, Seebeck coefficient, power factor and thermal conductance mentioned in Chapter 3.3. The transmission spectrum for electrons (phonons) is calculated by counting the number of channels in the corresponding energy (frequency) range.

By definition, conductivity gives the ratio of the conductance to cross-sectional area. However, in this study, the electrical and thermal conductances are calculated for the unit cell and they are divided by the width of the corresponding nanoribbon. Therefore, the given values are not the conductivities, but *the conductance per nanometer*. The conductance values given in Ref. (Özbal et al., 2019) are calculated in the similar way. The conductance values are scaled with respect to the width of the unit cell. The calculated Seebeck coefficient, power factor and the ZT values at 300 and 800 K are given in Table. A.2.

Table A.2. The calculated parameters of the single layer (SL-HfSe₂) and nanoribbon (NR) structures are; p- and n-type Seebeck coefficient, S ; power factor, P , thermoelectric figure of merit, ZT , and phonon thermal conductance per nm, κ_{ph} . Results of SL-HfSe₂ structure is from the Ref. (Özbal et al., 2019)

Structure	S ($10^{-4}V/K$)		P ($10^{-3}nW/K^2nm^2$)		ZT	
	300 K	800 K	300 K	800 K	300 K	800 K
SL-HfSe ₂	1.92 / -2.20	2.12 / -2.65	0.56 / 1.84	0.92 / 2.61	0.26 / 0.75	0.84 / 2.11
n=15	2.37 / -2.25	2.54 / -2.64	1.42 / 1.42	2.03 / 2.73	0.76 / 0.66	1.86 / 2.24
n=14	2.11 / -2.17	2.54 / -2.68	1.33 / 1.52	1.85 / 2.61	0.77 / 0.88	1.90 / 2.21
n=13	2.35 / -2.36	2.47 / -2.63	1.40 / 1.08	1.78 / 2.25	0.89 / 0.62	1.96 / 2.16
n=12	2.39 / -2.15	2.49 / -2.65	1.32 / 1.48	1.66 / 1.96	0.83 / 0.95	1.97 / 2.11
n=11	2.39 / -2.24	2.45 / -2.62	1.31 / 0.97	1.58 / 2.00	0.91 / 0.61	2.01 / 2.10
n=10	2.38 / -2.44	2.54 / -2.70	1.31 / 1.47	1.50 / 1.72	0.94 / 1.07	2.15 / 2.27
n=9	2.38 / -2.20	2.52 / -2.54	1.31 / 0.80	1.47 / 1.31	1.02 / 0.68	2.24 / 1.81
n=8	2.37 / -2.45	2.57 / -2.83	1.12 / 1.47	1.38 / 1.75	0.95 / 1.27	2.43 / 2.69
n=7	2.37 / -2.22	2.55 / -2.45	1.12 / 0.82	1.37 / 1.13	1.08 / 0.85	2.57 / 2.09
n=6	2.25 / -2.45	2.72 / -2.68	0.83 / 1.47	1.24 / 1.38	0.94 / 1.55	2.62 / 3.12

We also calculated Lorenz number for the NR structures. The calculated values are scaled with respect to the degenerate limit (Sommerfeld value) and the results are given in Table. A.3. Given L values correspond to chemical potential where ZT is maximum. As it is seen from the Table. A.3, the calculated Lorenz number for the NR structures are close to the theoretical value for the degenerate semiconductors ($2.44 \times 10^{-8}W\Omega K^{-2}$).

Table A.3. For nanoribbon (NR) structures, the calculated p- and n-type Lorenz numbers scaled with respect to the Sommerfeld value are given.

Structure	at 300 K		at 800 K	
	p-type	n-type	p-type	n-type
n=15	0.8	1.3	1.0	1.0
n=14	0.8	0.8	1.0	1.2
n=13	0.8	1.2	1.0	1.1
n=12	0.8	0.7	0.9	1.1
n=11	0.8	1.0	1.0	1.2
n=10	0.8	0.7	0.8	0.9
n=9	0.8	0.9	0.8	1.1
n=8	0.9	0.7	0.7	0.9
n=7	0.9	0.9	0.8	1.0
n=6	1.1	0.7	0.8	0.6

For the each NR structure, the electrical conductance G , Seebeck coefficient S , the thermal conductance of electrons κ_{el} , the power factor P and ZT are given as a function of

chemical potential μ in Fig. A.4 (for odd n) and Fig. A.5 (for even n). The thermoelectric properties are calculated for 300 and 800 K.

The band degeneracy in electronic spectrum of the NR structures with $n = 11$ and $n = 13$ reveals itself in the power factor results. These structures have two peaks near the conduction band edges and that causes an increment of the n-type ZT values. Except from these two structures, as the ribbon width increases the ZT value decreases and it converges to the two-dimensional limit.

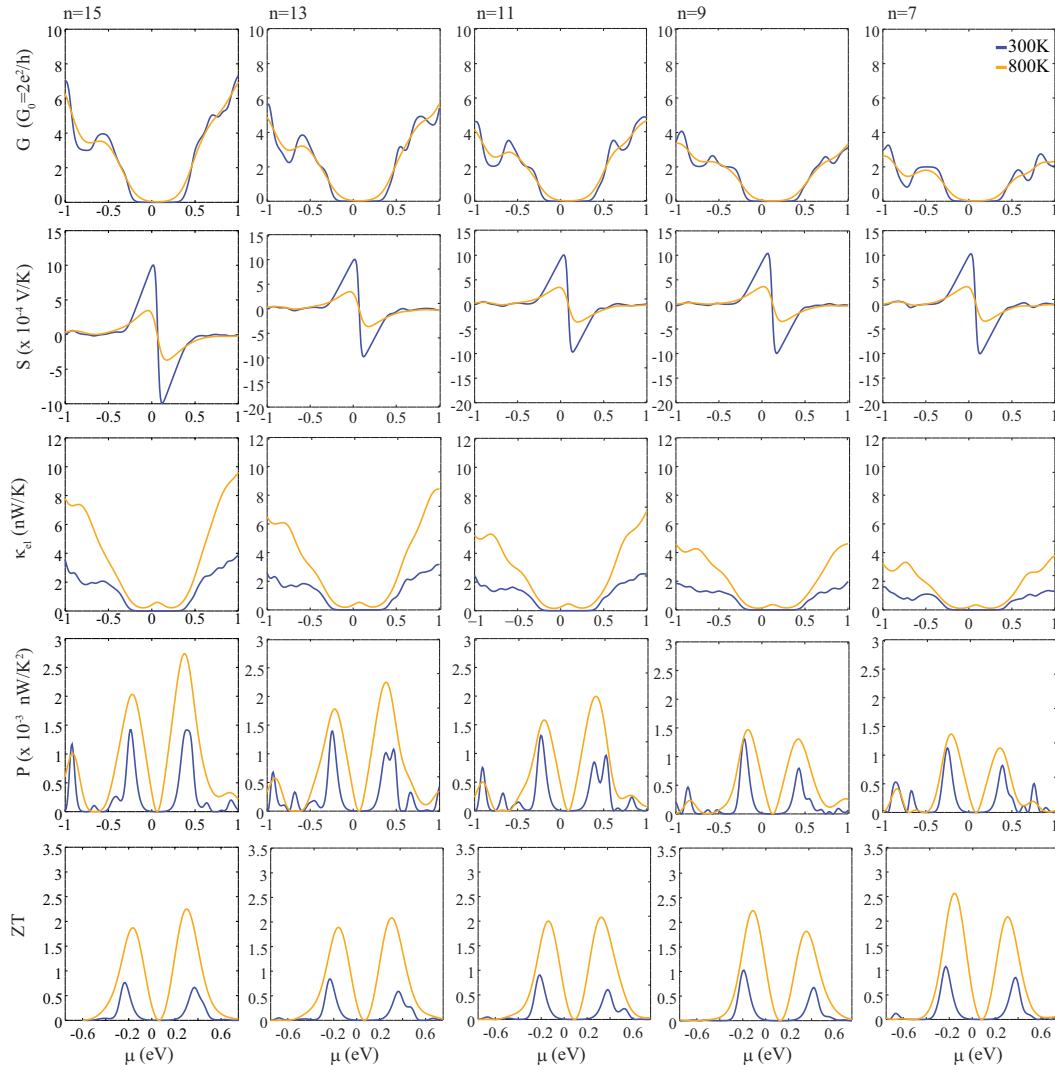


Figure A.4. The thermoelectric properties of the nanoribbon (NR) structures with odd n are given at 300 and 800K. The calculated parameters are; electrical conductance, G ; Seebeck coefficient, S ; thermal conductance of electrons, κ_{el} ; power factor, P ; and the thermoelectric figure of merit, ZT .

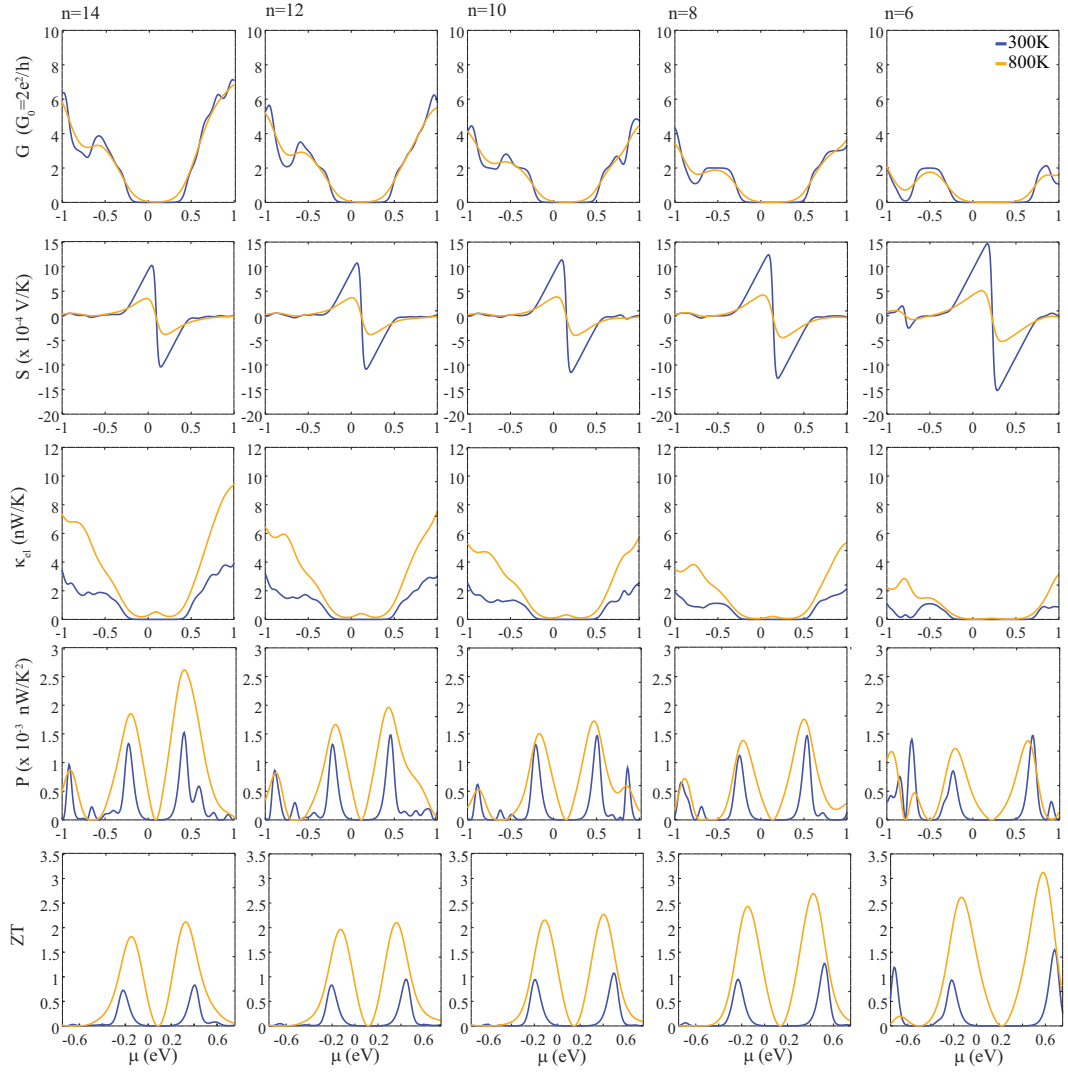


Figure A.5. The thermoelectric properties of the nanoribbon (NR) structures with even n are given at 300 and 800K. The calculated parameters are; electrical conductance, G ; Seebeck coefficient, S ; thermal conductance of electrons, κ_{el} ; power factor, P ; and the thermoelectric figure of merit, ZT .